ARMY RESEARCH LABORATORY

A Rod Ricochet Model

by Steven B. Segletes

ARL-TR-3257 **August 2004**

NOTICES

Disclaimers

The findings in this report are not to be construed as an official Department of the Army position unless so designated by other authorized documents.

Citation of manufacturer's or trade names does not constitute an official endorsement or approval of the use thereof.

Destroy this report when it is no longer needed. Do not return it to the originator.

Army Research Laboratory
Aberdeen Proving Ground, MD 21005-5066

ARL-TR-3257 **August 2004**

A Rod Ricochet Model

Steven B. Segletes
Weapons and Materials Research Directorate, ARL

Report Documentation Page

Form Approved
OMB No. 0704-0188

1. REPORT DATE *(DD-MM-YYYY)*	2. REPORT TYPE	3. DATES COVERED (From - To)
August 2004	Final	October 2001–March 2004

4. TITLE AND SUBTITLE
A Rod Ricochet Model

5a. CONTRACT NUMBER

5b. GRANT NUMBER

5c. PROGRAM ELEMENT NUMBER

6. AUTHOR(S)
Steven B. Segletes

5d. PROJECT NUMBER
AH80

5e. TASK NUMBER

5f. WORK UNIT NUMBER

7. PERFORMING ORGANIZATION NAME(S) AND ADDRESS(ES)
U.S. Army Research Laboratory
ATTN: AMSRD-ARL-WM-TD
Aberdeen Proving Ground, MD 21005-5066

8. PERFORMING ORGANIZATION REPORT NUMBER
ARL-TR-3257

9. SPONSORING/MONITORING AGENCY NAME(S) AND ADDRESS(ES)

10. SPONSOR/MONITOR'S ACRONYM(S)

11. SPONSOR/MONITOR'S REPORT NUMBER(S)

12. DISTRIBUTION/AVAILABILITY STATEMENT
Approved for public release; distribution is unlimited.

13. SUPPLEMENTARY NOTES

14. ABSTRACT
A model to predict the ballistic ricochet of rod penetrators is presented. The model is based on the premise that the phenomenology of ricochet is one where the impacting rod feeds into a plastic hinge located at the rod/target interface, and is thus diverted from a penetrating trajectory. The model is offered in both a full and simple form. The full form of the model arises from the simultaneous solution of a series of six algebraic equations that constitute the momentum-flux/force and moment balances upon the plastic hinge, subject to various material and kinematic constraints. This full model is not solvable in closed form, but rather by way of algorithm. The simple form of the model, by contrast, dispenses with the moment balance and makes several simplifying kinematic assumptions that permit the ricochet criterion to be expressed as a closed form inequality. Such a simplified form is along the lines of, and thus directly comparable to, several prior ricochet models in the literature. Compared against 24 ballistic tests, comprising two separate ricochet studies, the current model (in both forms) shows an improved ability to predict the ballistic ricochet of impacting rod projectiles. The simple form of the current ricochet model actually proved the best predictor of the ballistic data.

15. SUBJECT TERMS
ricochet, long rods, plastic hinge

16. SECURITY CLASSIFICATION OF:			17. LIMITATION OF ABSTRACT	18. NUMBER OF PAGES	19a. NAME OF RESPONSIBLE PERSON
a. REPORT	b. ABSTRACT	c. THIS PAGE			Steven B. Segletes
UNCLASSIFIED	UNCLASSIFIED	UNCLASSIFIED	UL	54	19b. TELEPHONE NUMBER (*Include area code*) 410-306-1939

Standard Form 298 (Rev. 8/98)
Prescribed by ANSI Std. Z39.18

Contents

List of Figures v

List of Tables vi

Acknowledgments vii

1. Introduction 1

2. Model Construct 5

2.1 Momentum and Moment of Momentum Balances....6

2.2 Plastic-Hinge Geometry....7

2.3 Stress and Strain Fields....9

2.3.1 Stress Field in Rod....9

2.3.2 Stress Field in Target....12

2.3.3 Strain Field in Rod....14

2.4 Bounding Constraints (Inequalities)....15

2.4.1 Flow Turning Angle....15

2.4.2 Angle of Reflection....16

2.4.3 Target Force Line of Action....16

2.5 Definitive Constraints (Equalities)....17

2.5.1 High-Flux Constraints....18

2.5.2 Low-Flux Constraints....19

2.6 Ballistic Response Criteria....20

3. Model Solutions 21

4. Observations on Model Behavior 26

4.1 Ricochet-Mode Transition....26

4.2 Behavior of Strain....27

4.3 Influence of Rod Aspect (L/D)....27

4.4 Nose-Shape Effects....27

4.5 Interaction Footprint Influence....28

5. Simplified Model With Closed-Form Solution **28**

6. Comparison to Other Models **32**

7. Comparison to Data **35**

8. Conclusions **40**

9. References **41**

Distribution List **43**

List of Figures

Figure 1. Spark cinematography of a ricocheting rod projectile, Senf *et al.* (*4*). 3

Figure 2. A macro-view of ricochet phenomenology, depicting forces and moments upon and fluxes through the plastic hinge contained within the shaded control volume of the rod. 6

Figure 3. View of plastic-hinge geometry, depicting kinematic variables s_1, s_2, x_s, and x_f, in terms of D, α, and θ. 8

Figure 4. Detailed stress field (σ, τ) in the rod's cross section at the onset of the plastic hinge, located at the control-volume boundary.....10

Figure 5. Schematic depiction of variables β and δ, along with a graphical depiction of their influence upon the respective net rod and target forces, f and F. 10

Figure 6. Detailed stress field (σ_T) imposed along elliptical bearing surface between target and rod. 13

Figure 7. Geometrical underpinnings of the $\alpha > |\eta|$ constraint.....17

Figure 8. Phase diagram of ballistic response as a function of H and θ, for engagement where ρ_R = 7800 kg/m^3, Y = 1 GPa, and V = 1000 m/s.....22

Figure 9. Phase diagram of ballistic response as a function of Y and θ, for engagement where ρ_R = 7800 kg/ m^3, H = 2 GPa, and V = 1000 m/s. 23

Figure 10. Phase diagram of ballistic response as a function of V and θ for engagement where ρ_R = 2700 kg/m^3, Y = 1.2 GPa, and H = 1.25 m/s. The figures depict (a) the rod response, (b) the target response, (c) the flux mode, and (d) integrated ricochet response. 24

Figure 11. Ricochet variables as a function of θ for the case where V = 700 m/s, ρ_R = 2700 kg/m^3, Y = 1.2 GPa, and H = 1.25 m/s. The figures depict (a) ricochet and line-of-force angles, (b) target forces and stresses, (c) strains, and (d) locations of stress-transition. 25

Figure 12. Comparison of full ricochet model to the simple model for prior cases where (a) H is varied, (b) Y is varied, and (c) V is varied. 31

Figure 13. Comparison of full ricochet model to the Tate model (*3*) for prior cases where (a) H is varied, (b) Y is varied, and (c) V is varied. 33

Figure 14. Comparison of full ricochet model to the Rosenberg model (*8*) for prior cases where (a) H is varied, (b) Y is varied, and (c) V is varied. 34

Figure 15. Results of B32 ricochet testing with comparison to ricochet/penetration predictions. 36

Figure 16. Results of L/D = 15 WA rod tests with comparison to ricochet/penetration predictions from the full-model currently proposed. 38

Figure 17. Comparison of model predictions for the current ricochet model (both full and simple forms), the Tate as well as the Rosenberg models against the results of L/D = 15-WA rod tests. 39

List of Tables

Table 1. Ballistic-response and ricochet mode designations. 21
Table 2. Experimental result for B32 test series. 36
Table 3. Experimental result for $L/D = 15$ tungsten-rod test series. 37

Acknowledgments

The author would like to thank the technician team of Experimental Facility 110 of U.S. Army Research Laboratory's (ARL's) Terminal Effects Division for executing the testing cited in this report. The author is also grateful to Dr. George Gazonas of ARL's Weapons and Materials Research Directorate for his review of this document.

INTENTIONALLY LEFT BLANK.

1. Introduction

The phenomenon of ricochet is an important consideration in ballistics. While a large fraction of laboratory-generated ballistic data are gathered under idealized impact-conditions of normal incidence, the physical and mathematically probable reality is that virtually all ballistic impacts on the battlefield occur at some nontrivial level of impact obliquity (as measured from the target normal). At low to moderate obliquity levels, the ballistic effect of the obliquity may only be that of an increased line-of-sight (LOS) thickness of the target. However, depending upon the material properties of the rod and target, the geometry of the rod, the impact velocity, and yaw, there will exist a critical angle of obliquity at and beyond which the rod ricochets from the target surface.

Ricochet has been a long studied phenomenon. An excellent review of work in the area is provided as a chapter in Goldsmith's review paper on projectile impact (*1*). Much of the research in ricochet centers on compact projectiles or else on rigid projectiles. A much smaller fraction of the work is focused on medium- and long-rod ricochet, where a different phenomenology often manifests itself.

Radiographic evidence and hydrocode simulation of long-rod ricochet was presented by Jonas and Zukas (*2*) in 1978. With experimental radiography and corroborating hydrocode simulation, they demonstrate how the rod can form a plastic hinge at the impact site (stationary with respect to the target) and deflect the rod from a rigid target surface. As the intent of Jonas and Zukas was to demonstrate a hydrocode modeling capability, no analytical modeling or analysis was offered.

In 1979, Tate (*3*) developed an early model for the ricochet of rods, in which the cylindrical rod (of square cross-section) responds as a rigid body away from the eroding tip. Tate's model allows for the local erosive deformation of the rod in the immediate vicinity of the impact. The asymmetric forces acting on this deforming rod tip are evaluated to ascertain their capacity to induce a rotation sufficient to bring about ricochet during the limited time before the rod tip becomes fully engaged in the target. While the model permits local deformation at the rod's tip, affecting the line of action of the interaction force, ricochet is judged to occur only if the remainder of the rod is adequately rotated, in a rigid fashion about its center of gravity, so as to produce a net linear velocity in the rod tip parallel to the target surface. Tate's approach produces an analytical expression for the target obliquity angle θ_{CRIT}, beyond which ricochet is predicted to occur. That expression is given as

Tate Model:

$$\tan^3\theta_{\mathrm{CRIT}} > \frac{2}{3}\frac{\rho_R V^2}{Y}\frac{L^2+D^2}{LD}\frac{V}{V-U}, \tag{1}$$

where ρ_R is the rod's density, V is the striking velocity of the rod, Y is the yield strength of the rod, L and D are the rod's length and diameter, respectively, and U is the initial penetration velocity of the rod into the target. The analysis is based upon the impact of flat-nosed projectiles. Note that the need for the penetration velocity U as input to the model requires an auxiliary calculation from a ballistic penetration model, such that U, in addition to the rod variables already listed, becomes a function of the target resistance H and the target density.

One of the drawbacks of the Tate ricochet model is its failure to predict ricochet for the rigid-rod (*i.e.*, $U = V$) scenario because of the method used to calculate the line of action of the interaction force. Further, because of the model's requirement to ricochet by way of rigid-rod rotation, ricochet becomes increasingly improbable as the rod length is increased. The empirical observation of a plastic hinge in the rod does not play into the modeling phenomenology of the Tate ricochet model. While perhaps relevant for lower velocity impacts, Tate's model tends to require very high obliquities to predict ricochet, precisely because the model assumes a rigid-rod response in which the complete rod must acquire rotational motion, about its center of mass, in order for the rod nose to acquire its needed deflection velocity.

Like Jonas and Zukas (*2*), Senf *et al.* (*4*) similarly showed in 1981 how the ricocheting rod can form a plastic hinge at the impact site to deflect the rod from a rigid target surface (figure 1). Such observations provided additional evidence that, even in the absence of erosion, a rigid rod assumption does not necessarily hold during the ricochet process. Like Jonas and Zukas, the intent of Senf *et al.* was to demonstrate hydrocode modeling capability, and so no additional analysis was offered. One important point to draw from their result, in distinction to Tate's ricochet modeling, is that, when this plastic-hinge phenomenology is operational, an increase in the length of the rod is not necessarily an impediment to ricochet.

Reid *et al.* (*5*) began to address, with analysis, the notion of the plastic hinge, traveling down the rod's length, but stationary with respect to the target surface. In their analysis, they simplified the problem to consider only the transverse bending forces and were able to analogize the problem to one of a transverse impact on the free end of a cantilever beam. As such, their solution falls in the realm of mechanics of materials, and does not consider issues of momentum flux through the hinge region, which will be shown to exert influence at higher striking velocities. From their analysis, they are able to predict that the hinge is able to progress down the rod only 41% of its length, before being arrested as the rod acquires the same rotational velocity as the material in the hinge. While such an analysis helped to explain their own experimental data, it is at odds with the higher velocity experiments of Jonas and Zukas (*2*) and Senf *et al.* (*4*), wherein the hinge was observed to traverse the full length of the rod.

Johnson *et al.* (*6*) studied ricochet interactions of plasticine (modeling clay) rods and targets. Based upon predictions from Tate's ricochet model (*3*), Johnson *et al.* limited their testing to impact obliquities above 75°. Photographic records of their testing reveal plastic-hinge behavior similar to that reported by Jonas and Zukas (*2*) and Senf *et al.* (*4*). Despite this missed

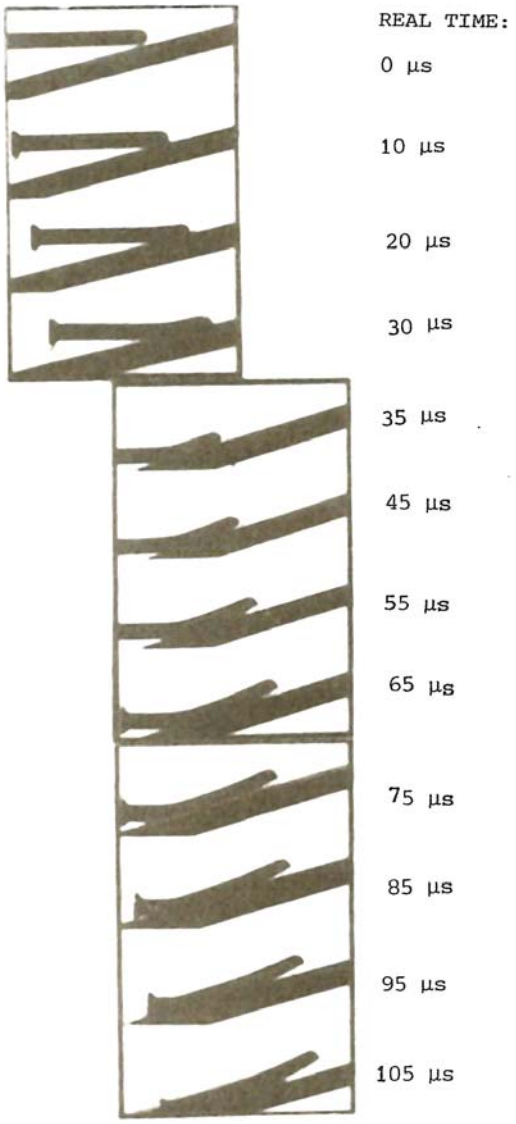

Figure 1. Spark cinematography of a ricocheting rod projectile, Senf *et al.* (*4*).

opportunity to critically test aspects of the Tate model, the authors nonetheless conclude that "test results generally confirm [the Tate ricochet] equation" (even though ricochet by way of plastic hinge is not part of the Tate ricochet methodology). Beyond correlation with the Tate model, empirical relations were presented between target imprint dimensions and striking velocity, as well as some time history data from specific tests.

By 1983, several of the authors previously examining the ricochet problem combined efforts to produce new results. The work of Johnson *et al.* (*7*) continued with the impact of plasticine rods, this time upon rigid targets, with new analysis brought to bear on the problem. The impact

velocities were very low and impact obliquities were restricted to angles below 60°. Their work seems to focus more on the related but distinct problem of rod buckling as the primary mode of deformation, rather than bending associated with ricochet deflection.

Rosenberg *et al.* (*8*) revisited the ricochet problem in 1989. They acknowledged adapting many of Tate's (*3*) original premises, concerning the origins of the asymmetric force that acts upon the eroding tip of the impinging rod, as well as the assumed square cross section of the rod. However, the key point of departure for Rosenberg *et al.* is in assuming that the interaction force acts only upon the mass actively engaging the target, and not upon the wholly remaining rigid rod as Tate assumed. Thus, in the Rosenberg model, the interaction force acts to linearly deflect rod-tip material in the transverse direction, rather than acting to apply a rotational moment upon the rigid rod, as in the Tate ricohet model. This alteration, the authors indicate, is to account for "bending rods," an allusion to the plastic-hinge phenomenon observed during rod ricochet by many authors. The resulting ricochet criterion is given as

Rosenberg Model:

$$\tan^2 \theta_{\text{CRIT}} > \frac{\rho_R V^2}{H} \frac{V+U}{V-U}, \tag{2}$$

where H is the target resistance. Like Tate's model, the Rosenberg model's need for the penetration velocity U as input demands a further calculation that requires, in addition to those variables listed, knowledge of the rod strength Y and the target density. The model was shown to have good prediction ability for length-to-diameter (L/D) ratio = 10 tungsten (W) rods launched against rolled homogeneous armor (RHA) targets at striking velocities between 600 and 1400 m/s and target obliquities between 55 and 75°.

The interaction methodology of Rosenberg *et al.*, however, calculates the force interaction based upon a virgin, flat-nosed rod striking an erodible (but as yet undeformed) target. Thus, it would seem that the methodology should only offer a prediction as to what happens to the initial flux of rod material against the target. Once the initial tip of rod is deflected, for example, the geometric "initial conditions" of the remaining rod and gouged target surface are no longer in harmony with the model's assumptions. Such a situation indicates that the model would be unable to predict observed cases wherein the rod's tip is sloughed off via ricochet followed by the remaining rod shank establishing penetration. And like Tate's model from which it derived, the methodology breaks down under conditions in which the rod remains rigid (*i.e.*, when $U = V$) because of the manner in which the interaction force's line of action is calculated.

More recent studies of the ricochet phenomenon focus on spherical projectiles (*9*), rigid projectiles (*10*), computational methods (*11*), or else touch on ricochet only peripherally as part of a larger examination (*12*, *13*). None of these studies offer additional analytical modeling insight into the phenomenology of medium- and long-rod ricochet.

2. Model Construct

In this report, a new ricochet model is developed and presented. The fundamental premise of the proposed model is the assumption (borne out by repeated observation [*2*, *4*, *6*]) that ricochet occurs via a plastic hinge in the rod, located at, and stationary with respect to, the target interface, into which the moving rod feeds itself. Unlike a mechanics-of-materials-based approach, the proposed model accounts for the momentum fluxes that enter and leave the hinge region. And unlike approaches that seek to ascertain ricochet by examining the rod/target force interaction in the first few microseconds of impact, the current model bases its ricochet judgment on the answer to a different question: can the interaction stresses and fluxes in the rod and target produce the forces and moments required to continuously sustain a plastic hinge at the rod target interface?

While such an approach can be criticized for ignoring key influences, like the rod's nose shape, other ricochet models likewise limit their utility by basing their predictions on one particular nose shape, namely, a flat-nosed rod. Another deficiency of the current approach is the assumption that the rod is massive and long enough to ensure no change over time in the rod's engagement-yaw angle, despite the interaction moment applied to the rod at the hinge. In truth, any rotation of the rod prior to the moment that penetration is firmly established only aids the propensity to ricochet. While such rotations are most significant for shorter rods, where the moment of rotational inertia is small, the current approach will nonetheless be unable to predict changes in the rod-pitch characteristics that might occur over the course of a single ballistic event. In spite of this, or more precisely, because of it, the model should provide a conservative estimate of a rod's propensity to ricochet (*i.e.*, ricochet will be at least as likely as the model predicts.)

While analytically based, the full model cannot, unfortunately, be distilled down to a single inequality, as can the models of Tate (*3*) or Rosenberg *et al.* (*8*) (however, a simplified version of the full model will be discussed later in this report.) Nonetheless, the full model is represented by a handful of algebraic equations that must be simultaneously solved, subject to various constraints. The algorithm was coded so that the predictive envelope of the model could be explored.

Examining in figure 2 the macroscopic view of a ricochet event resulting from a steady-state plastic hinge, one may note some of the defining constructs of the proposed model. All forces and moments shown in the figure represent forces and moments acting upon a control volume (shown shaded) of rod material that extends from the leading edge of the plastic hinge to the point where the ricocheted material becomes free-flying. Along the length of the hinge, the target interacts with the rod material within the plastic hinge over an elliptical area of the target surface described by the projection of the rod's cross section onto the target's (original) surface.

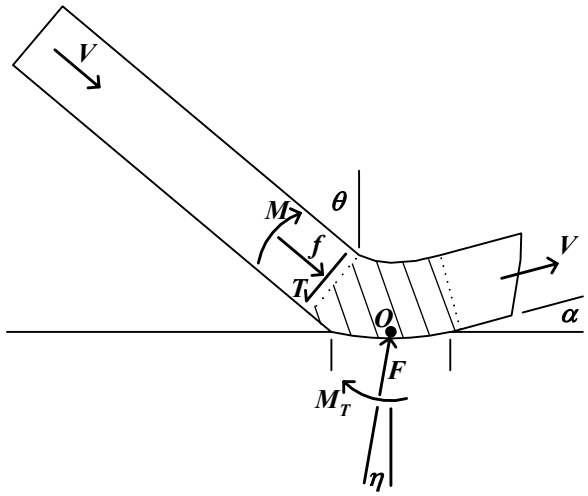

Figure 2. A macro-view of ricochet phenomenology, depicting forces and moments upon and fluxes through the plastic hinge contained within the shaded control volume of the rod.

The center of this interaction ellipse is designated as point *O* and represents the intersection of the rod's central axis with the target's original surface.

Referring to this figure, the circular cross-section rod, of density ρ_R, impacting with velocity V, at an angle of obliquity θ, applies some net level of compressive force f along the axis of rod (which intersects point *O*), upon the leading edge of the hinge. There is also a clockwise bending moment M, about *O*, applied at the hinge's leading edge, due to the stress-field gradient associated with rod bending at that location. While the method does not solve the problem for the general multi-axial stress field, there are certain low-flux cases where accounting for the shearing traction T across the leading edge of the hinge becomes necessary, as well. The trailing edge of the control volume (just beyond the plastic hinge), through which the ricocheted material exits, is assumed to be stress free. Ricocheted material leaves the hinge with the same velocity it entered, namely V, representing a net rate of mass flux through the hinge of dm/dt mass per unit time. The ricocheted material exits upon a trajectory at angle α with respect to the target surface. To the hinge, the target applies a compressive load of magnitude F through point *O*. Allowing that the target may be plastically gouged under the elliptical footprint, the target force may be acting on a line at an angle η with respect to the target surface. A positive moment M_T, about *O*, will arise if the target's stress field is skewed to the leading edge of the elliptical footprint of interaction. The target moment may be positive, zero or negative, depending on the skew of the target stress field within the elliptical interaction footprint.

2.1 Momentum and Moment of Momentum Balances

Even without specifying the detailed nature of the stress fields at this point (*i.e.*, limiting the view of ricochet to that presented in figure 2), the momentum and moment of momentum

balances may be composed by employing standard momentum analyses upon the shaded control volume of figure 2:

Force/momentum-flux normal to f:

$$F\sin(\theta+\eta) = T + V\dot{m}\cos(\theta-\alpha)\,, \tag{3}$$

force/momentum-flux normal to F:

$$f\sin(\theta+\eta) = T\cos(\theta+\eta) + V\dot{m}\left[\cos(\alpha+\eta) - \sin(\theta+\eta)\right], \tag{4}$$

moment of momentum about O:

$$M + M_T = T x_s + x_f V\dot{m}\,. \tag{5}$$

In equation 5, the term x_s represents the perpendicular distance from point O to the face of the leading edge of the control volume (where shear traction T acts), and x_f is the perpendicular distance from point O to the central trajectory axis of the ricocheting material (the line of action of the momentum efflux). In all these equations, the momentum flux entering and exiting the control volume may be calculated as

$$V\dot{m} = \rho_R V^2 A_0\,, \tag{6}$$

where A_0 is the cross-sectional area of the rod, equal to $\pi D^2/4$. Equations 3–5 are the primary equations to be solved, with unknowns f, F, T, M, M_T, α, and η. Clearly, linkages between and constraints upon these variables will need to be constructed in order to obtain a solution. While yet unknown, the distances x_s and x_f are calculable from geometric considerations.

2.2 Plastic-Hinge Geometry

A characterization of the plastic-hinge geometry needs to be put forth, in order to specify the distances x_s and x_f, which are moment arms for the shear traction and momentum efflux, respectively. Furthermore, a specification of the hinge geometry will also be useful later in calculating the strains present within the plastic hinge. The knowledge of strains in the rod may be used as an estimate as to whether a ricocheting rod retains its integrity as a rod, or alternately breaks into a spray of ricocheting fragments.

Fully consistent with strength-of-materials beam theory, the starting and ending boundaries of the plastic hinge may be specified as planes perpendicular to the symmetry axes of the striking and ricocheting rod, respectively. Beyond this, the sole geometric assumption that constrains the plastic hinge location is that the hinge be confined to distance from the target surface exactly equal to one rod diameter D (figure 3). The reasoning is as follows: as the ricocheting rod material within the hinge changes its trajectory through an angle of $\pi/2 - \theta + \alpha$, it will at some point in that process flow parallel with the surface of the target plate (and the associated rod cross section will thus be perpendicular to the target surface.) If the rod does not flatten significantly during the ricochet process, and if any plastic deformation of the target remains

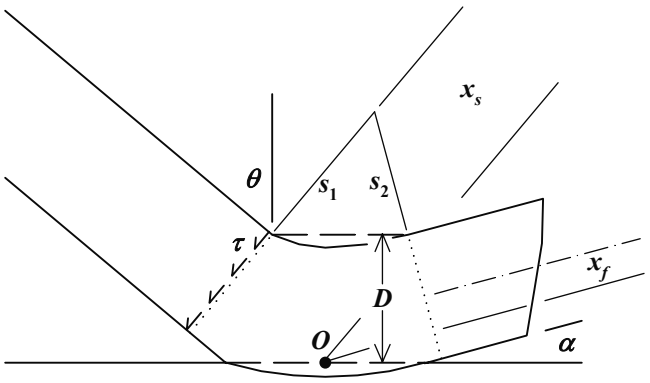

Figure 3. View of plastic-hinge geometry, depicting kinematic variables s_1, s_2, x_s, and x_f, in terms of D, α, and θ.

measurably small, the rod cross section at that point in the hinge will necessarily span the distance from the target surface to a distance D from the surface. It seems kinematically unlikely, then, that there would simultaneously exist an elastic rod cross section (outside of the hinge) that is fully entrained within a distance less than D from the surface. This assumption, therefore, merely reflects the reasoning that any cross section of the rod fully entrained within a rod-diameter's distance from the target is very likely in a plastic state and is thus part of the hinge.

With this geometric assumption in place, the moment arms for the shear traction and momentum efflux, used in equation 5, may be determined, respectively, from figure 3 as

$$x_s = D\left(\frac{1}{\cos\theta} - \frac{\tan\theta}{2}\right), \tag{7}$$

and

$$x_f = \frac{D}{2}\left(1 - \frac{\sin\alpha}{\cos\theta}\right). \tag{8}$$

It is seen that, while x_s is fully determined from the striking conditions of the impact, the value of x_f is dependent upon the unknown ricochet angle, α.

Likewise, from figure 3, the distances from the leading and trailing edges of the hinge to the average center of curvature for the hinge may also be determined, respectively, as

$$s_1 = \frac{D}{\cos\theta}\frac{\left[\tan\theta - \tan(\alpha/2)\right]}{\left(1 + \tan\theta\tan\alpha\right)} \tag{9}$$

and

$$s_2 = s_1 \frac{\sin\theta}{\cos\alpha}. \tag{10}$$

These values will later be used as part of a strain calculation.

2.3 Stress and Strain Fields

While the macroscopic view of figure 2 shows the forces and moments acting upon the control volume, it must be appreciated that these net forces and moments arise out of the detailed stress fields that are applied to the surface of the control volume. While this model does not propose to solve exactly for what those stress fields must be, certain reasonable assumptions may be asserted as to the general form they take. The specification of these stress field forms will permit their integration over surface areas of the control volume to yield the macroscopic forces (f, F, T) and moments (M, M_T) that enter into the momentum balances of equations 3–5.

Knowledge of strain fields, on the other hand, is not required in determining whether a ricochet solution is viable. However, if a viable ricochet solution is found, the geometry of the resulting hinge may be used to estimate the local strain field in the rod. Knowledge of this strain field and the material's strain-to-failure properties, in turn, can provide useful information to estimate, for example, whether the ricocheting rod will retain the integrity of an intact rod, or whether it is likely to fracture into a spray of deflecting fragments. Such knowledge would be useful in ascertaining the lethality of a threat projectile in a post-ricochet condition.

2.3.1 Stress Field in Rod

In traditional strength-of-materials theory, a plastic hinge that results from pure bending in a circular cross-section beam acquires a stress field in which exactly half of the beam's cross section is in compression and half in tension. In order for the stress state to represent a plastic hinge, all fibers in the cross section must be at the yielding stress Y. And thus, the full cross section acquires a normal stress magnitude σ equal to Y, half of it in compression and half in tension. Such a stress state produces a cross section that is in pure bending.

In the case of an impacting rod, however, one expects an axial compressive component resulting from inertia of the decelerating rod as it strikes the target. The proposed stress-state distribution that will allow both the presence of a plastic hinge, as well as a net axial force component f is described in figure 4. In this cross section, all material elements possess a stress magnitude σ at the yield point, necessary to facilitate a plastic hinge. However, unlike the traditional hinge, the fraction of the rod cross section under compression will not equal exactly 0.5, but rather fall in the range of 0.5–1.0, in order to produce a net axial compressive force f perpendicular to the cross section.

The variable that will be used here to define the divide between compression and tension in the cross section will be the angle β which, as seen in figure 5, represents the half angle with vertex

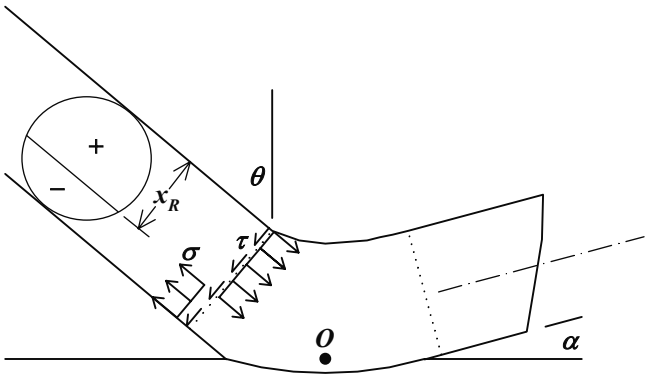

Figure 4. Detailed stress field (σ, τ) in the rod's cross section at the onset of the plastic hinge, located at the control-volume boundary.

at the center of the rod's cross section, such that 2β is fully subtended by the tensile region of the cross section. In order for the net force on the cross section to remain compressive, the angle β will fall in the range of 0 (full compression) to $\pi/2$ (equal compression and tension). When the rod cross section is in full compression ($\beta = 0$) and in the absence of shear stress, the axial force f in the rod will be its maximum limiting value,

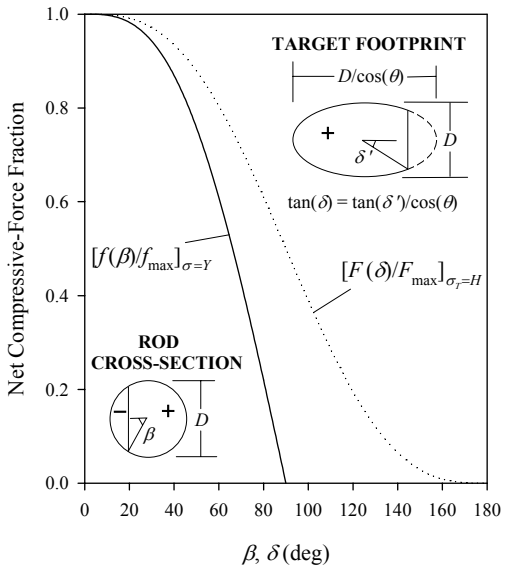

Figure 5. Schematic depiction of variables β and δ, along with a graphical depiction of their influence upon the respective net rod and target forces, f and F.

$$f_{\max} = YA_0 . \tag{11}$$

In general, however, the fraction of the rod diameter under compression may be given as

$$\frac{x_R}{D} = \frac{1}{2}\left(1 + \cos\beta\right), \tag{12}$$

which dictates that $x_R \geq D/2$ always. The net compressive force on the cross section, relative to $f_{\max}$, is given through integration as

$$\frac{f}{f_{\max}} = \frac{\sigma}{Y}\left[1 - \frac{1}{\pi}\left(2\beta - \sin 2\beta\right)\right], \tag{13}$$

as depicted in figure 5. Similarly, a specification of β will define not only the axial rod force, but also the moment about the cross section's neutral axis (the diameter dividing the cross section in two equal semicircles):

$$\frac{M}{f_{\max} \cdot D} = \frac{\sigma}{Y}\frac{2}{3\pi}\sin^2\beta . \tag{14}$$

The rod's net moment has been nondimensionalized by the product of the limiting rod force and rod diameter. Because the axial stresses are acting perpendicular to the cross section, and point *O* in figure 2 was defined to represent the intersection of the rod's central axis with the target surface, the moment *M* about the cross section's neutral axis given in equation 14 is identical to the moment of these stresses acting about point *O*. In the sense of figure 2, the moment *M* will always be positive in magnitude.

In addition to the angle β exerting influence upon the axial force and moment, the axial-stress-state magnitude σ in the rod plays a role, as well. While the basic tenet of a plastic hinge requires the stress state at all points in the cross section to be at yield, the presence of a multiaxial stress state (*e.g.*, the presence of shear stress τ) will lower the axial component σ below the value of yield stress *Y*. In particular, for the biaxial stress state envisioned, the relationship between σ, τ, and *Y* is governed from standard theory as

$$\frac{\tau}{Y} = c\sqrt{1 - \left(\frac{\sigma}{Y}\right)^2} , \tag{15}$$

where $c = 1/2$ for materials obeying a Tresca yield condition, or $c = 1/\sqrt{3}$ for when the von Mises yield condition is applicable. It is this shear stress τ, assumed for simplicity to be uniformly distributed over the cross section, which comprises the shear traction *T* depicted in figure 2, according to the relation

$$T = \tau A_0 . \tag{16}$$

2.3.2 Stress Field in Target

As cited already, the interaction zone where the ricocheting rod and target interact is assumed to be limited to an elliptical footprint formed by projecting the rod's circular cross section onto the target surface. Such an ellipse has an eccentricity of $\sin\theta$ and area $A_0/\cos\theta$. The center of this ellipse is denoted as point *O*, and also lies along the rod's axis of symmetry. When the target response is elastic, the interaction footprint represents (within the bounds of elastic deformation) the actual surface over which the actual compressive target stress σ_T may be applied to produce a net target force *F* normal to the target surface.

The model also allows for a nonelastic target response, in which the net target force *F* is applied at an angle η with respect to the target normal, as shown in figure 2. This condition is intended to represent the case where the target surface, as a result of the interaction with the rod, develops a significant surface gouge. While, in reality, the actual stress increments are applied normal to this continuously varying gouge surface, the idealization here is that the bearing surface of the gouge may be effectively represented by a secondary ellipse, which is canted at an angle η with respect to the interaction ellipse on the target surface and whose normal projection is exactly onto the interaction ellipse on the target surface. This secondary ellipse (the bearing surface) will always be smaller than (or equal to) the interaction ellipse on the target surface. Its area is given by $A_0\cos\eta/\cos\theta$, with minor axis of length *D* and major axis of length $D\cos\eta/\cos\theta$. When η is identically zero (the elastic case), the target's bearing surface and the interaction ellipse coincide. Thus, the maximum force that may be applied by the target to the ricochet bearing surface will be given as

$$F_{\max} = HA_0 \frac{\cos\eta}{\cos\theta}. \tag{17}$$

Equation 17 reveals that all other things equal, under this idealization, the allowable target force diminishes by a factor of $\cos\eta$ when the target is gouged. While it might seem that such configurations are less prone to ricochet because of the lesser forces that can be supported, the reality is that the reorientation of the target force's line of action by an angle η may actually decrease the magnitude of force required for ricochet to an extent where an elastically untenable ricochet becomes viable if the target is permitted to gouge.

While the true interaction no doubt produces a complicated stress field on the bearing surface, the stress-field idealization employed for the target in this analysis is two-fold: that any stress applied on the target's planar bearing surface will be a uniform normal compressive stress of magnitude σ_T; but that the actual area upon the elliptical bearing surface over which this normal compressive stress is applied could be a truncated fraction of the total bearing ellipse, with the truncation line being drawn parallel to the minor axis of the elliptical bearing surface (figure 6). Analogous to the technique used to define the stress state in the rod's cross section, the angle $2\delta''$ can be defined as the central angle fully subtended by the truncated region of the bearing surface ellipse. If the truncated region encompasses the trailing edge of the ballistic interaction, such

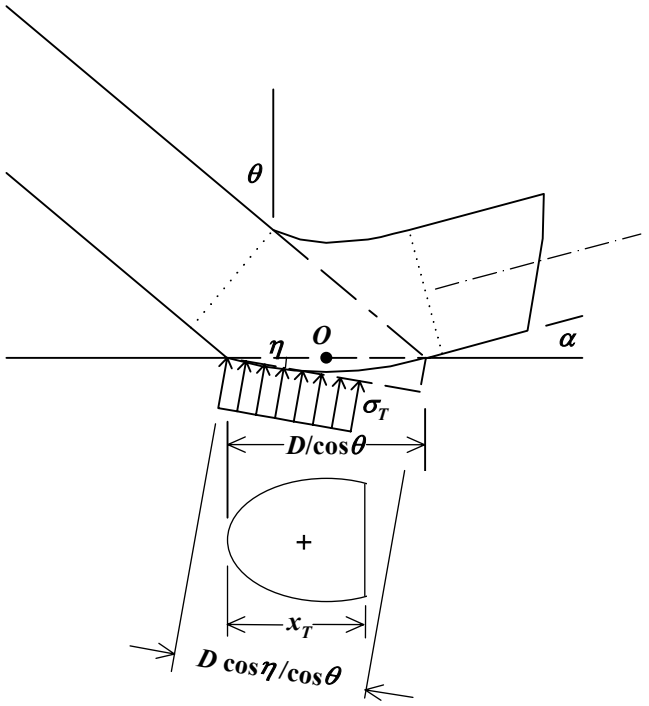

Figure 6. Detailed stress field (σ_T) imposed along elliptical bearing surface between target and rod.

that the net force is skewed to the leading edge of the bearing surface, a net positive moment M_T will be applied about center of the bearing surface ellipse (and thus about point O). If the truncation encompasses the leading edge of ballistic interaction, the target moment M_T, about O, will have negative sign.

When the bearing surface is projected normal to itself upon the interaction ellipse on the target surface, the bearing surface angle δ'' becomes, in the projection, δ', according to the relation $\tan\delta' = \tan\delta''\cos\eta$. Likewise, when this truncated interaction ellipse is projected along the rod axis to a plane perpendicular to the rod's axis, the interaction ellipse transforms to a circle, and the truncation angle δ' becomes δ in this circle, according to the relation $\tan\delta' = \tan\delta\cos\theta$. These geometric transformations from δ'' to δ, by way of the combined transformation $\tan\delta = \tan\delta''\cos\eta/\cos\theta$, permit the mathematical relations developed for circular cross sections in equations 12–14 for the rod to be applied analogously to the elliptical bearing surface of the target, with a few notable differences. For one, while the rod cross section has zones in compression and tension, the target's bearing surface has zones in compression or alternately stress free. Secondly, the angle β in the rod equations was limited in range to $\pi/2$, in order to constrain the rod to a net positive force f, whereas the range of δ may span from 0 to π while still keeping the net target force F in compression, as depicted in figure 5.

In terms of the transformed truncation angle δ and normalized by the limiting target-bearing force F_{max}, the force applied to the truncated bearing surface is

$$\frac{F}{F_{\max}} = \frac{\sigma_T}{H}\left[1 - \frac{1}{2\pi}\left(2\delta - \sin 2\delta\right)\right], \tag{18}$$

as shown in figure 5. Analogously, the magnitude of the moment of the target-bearing stresses about point *O* is given as

$$\frac{\left|M_T\right|}{F_{\max} \cdot D\cos\eta/\cos\theta} = \frac{\sigma_T}{H}\frac{1}{3\pi}\sin^2\delta\,. \tag{19}$$

Here, the target moment is nondimensionalized by the product of the limiting target force and bearing surface's major-axis dimension. Again, the actual sign of the moment depends on whether the target stresses are skewed to the leading edge of the bearing surface (positive M_T) or to the trailing edge (negative M_T).

Finally, the fraction of the major axis from the target's interaction footprint that is under load is given by

$$\frac{x_T}{D/\cos\theta} = \frac{1}{2}\left(1 + \cos\delta\right). \tag{20}$$

2.3.3 Strain Field in Rod

The strain field in the ricocheting rod may be estimated from the geometry of the hinge. The distances s_1 and s_2 from the center of curvature of the hinge to the leading and trailing edges of the hinge were calculated in equations 9 and 10, and shown in figure 3. The neutral fiber (line of zero stress), at the leading edge of the hinge, is therefore at a radius of curvature of $s_1 + x_R$ (where x_R is defined in equation 12.) Similarly, the neutral fiber at the trailing edge of the hinge, in the absence of axial stress, is at a radius of $s_2 + D/2$.

Certain quantities, averaged over the plastic hinge, may be developed. The radius of curvature to the average neutral fiber may be give by *R*, defined as

$$R = \frac{(s_1 + x_R) + (s_2 + D/2)}{2}. \tag{21}$$

Because the flow in the hinge turns through an angle of $\pi/2 - \theta + \alpha$, the estimated length of the neutral fiber over the extent of the hinge is

$$l_0 = R(\pi/2 - \theta + \alpha)\,. \tag{22}$$

The radius of curvature of the neutral fiber, over the extent of the hinge, changes by a value of

$$\Delta R = (s_1 + x_R) - (s_2 + D/2)\,. \tag{23}$$

Thus, as a material element traverses a length l_0 over the length of the hinge, it distorts in the transverse direction by a distance ΔR. The tensorial plastic shear strain (*i.e.*, one half the total shearing angle) that occurs within the hinge is therefore

$$\varepsilon_{xy} = \frac{1}{2}\tan^{-1}\left(\frac{\Delta R}{l_0}\right). \tag{24}$$

Turning to the normal strain components, the average radius of curvature to the rod fiber under greatest compression (along those fibers closest to the center of curvature) may be given by $\bar{s}$, defined as

$$\bar{s} = \frac{s_1 + s_2}{2}, \tag{25}$$

while the average radius of curvature to the rod fiber under greatest tension (along those fibers farthest from the center of curvature) is $\bar{s} + D$. Thus, the maximum compressive plastic strain in the hinge may be given as

$$\varepsilon_x^c = \ln(\bar{s}/R), \tag{26}$$

while the maximum tensile plastic strain is specifiable as

$$\varepsilon_x^t = \ln[(\bar{s}+D)/R]. \tag{27}$$

Because the neutral bending fiber in the rod, at radius of curvature R, will always be closer to the tensile boundary of the rod's cross section (in order to keep the rod in net axial compression), the maximum compressive strain will always exceed in magnitude the maximum tensile strain. Thus, the maximum equivalent plastic strain in the rod (assuming plastic incompressibility) occurs in the compressed fiber of the rod closest to the hinge's center of curvature, and may be given as

$$\bar{\varepsilon}_{\max} = \sqrt{\varepsilon_x^{c2} + 4/3 \cdot \varepsilon_{xy}^2}. \tag{28}$$

By comparing these calculated strain values within the plastic hinge to the rod material's strain-to-failure properties, an indication may be obtained of whether the ricocheting rod is likely to remain an intact rod or break into a spray of deflected fragments.

2.4 Bounding Constraints (Inequalities)

The following constraints provide bounds on some of the variables. While not diminishing the number of problem unknowns, these constraints aid the solution by narrowing the domain over which valid solutions may be sought.

2.4.1 Flow Turning Angle

The total flow-turning angle $\pi/2 - \theta + \alpha$ of a ricocheting rod is limited to an angle less than or equal to $\pi/2$. This may be restated as

$$\alpha \leq \theta. \tag{29}$$

The basis for this constraint is that, from the perspective of simple momentum transfer, the propensity of an impacting rod to dwell (*i.e.*, flow-split, or pancake) on the target surface (with individual material particles turning through an angle $\pi/2$ or less would prevail before a rod would tend to ricochet through an angle greater than $\pi/2$.

It was earlier shown that $x_R \geq D/2$. Additionally, with equations 10 and 29, it may now be shown that $s_1 \geq s_2$. One may thus conclude that the transverse (shearing) displacement in the hinge, ΔR, from equation 23 will always be positive (implying a net counter-clockwise shearing moment in the sense of figure 2). Such a conclusion implies that the shearing traction T on the plastic zone must always be positive in magnitude in order to produce the net counter-clockwise shearing moment about O per the sense of figure 2.

2.4.2 Angle of Reflection

The angle of reflection of a ricocheting rod will be less than or equal to the angle of striking incidence. This criterion may be stated as

$$\alpha \leq \pi/2 - \theta . \tag{30}$$

The basis for this constraint is that, for a strength-free rod made to ricochet off a rigid target, the angle of reflection will exactly equal the angle of incidence. The addition of rod strength to the picture can only mitigate the angle of flow turning, which will therefore limit the angle of ricochet reflection to a value at or below the angle of striking incidence.

2.4.3 Target Force Line of Action

When the equations were developed for the stresses and forces developed by the target upon the ricocheting rod, an artifice was developed for the case of a plastic target response, in the form of a target-load bearing surface, canted by an angle η with respect to the target surface. It was noted that the bearing surface was an idealization to represent the case where the target surface develops a significant surface gouge. While, in reality, actual force increments are applied normal to this continuously varying gouge surface, the idealization posits that the target stresses are coaligned, perpendicular to the canted, and planar bearing surface. Such an idealization permits rapid integration of the net force F from the idealized stress field.

The artifice of this canted bearing surface notwithstanding, the geometry of an actual gouge is seen to place an additional constraint on the ricochet process. If an actual (assumed symmetric) ricochet gouge forms, such that an angle ξ is formed at the gouge lip with respect to the target-surface plane, then the surface normals throughout the gouge will span the angular range of $-\xi$ to $+\xi$ with respect to the target normal (figure 7). The line of action of the net target force F (which acts at angle η), being an integration of the normal forces increments dF over the actual bearing surface (the gouged crater), must also fall in the range $-\xi$ to $+\xi$, because there are no force increments having a line of action outside of this range. Thus, $|\eta| \leq \xi$.

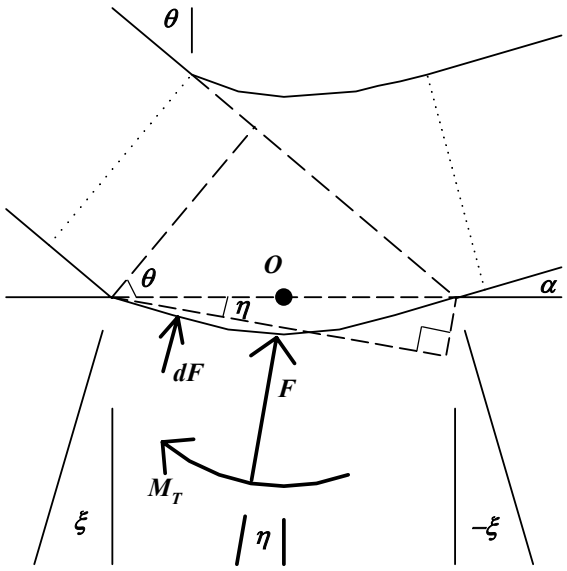

Figure 7. Geometrical underpinnings of the $\alpha > |\eta|$ constraint.

With respect to the trajectory of material exiting this gouged crater, the material scraping its way along the shallow crater toward the trailing edge of the gouge would exit the gouge with a trajectory aligned at an angle ξ (or $> \xi$ if it "bounced" off the gouge) with respect to the surface of the target. This exit trajectory is defined by the angle α, and thus $\alpha \geq \xi$.

Combining these two results yields an additional bounding constraint on the solution of the ricochet equations, namely

$$|\eta| \leq \alpha. \tag{31}$$

2.5 Definitive Constraints (Equalities)

With the descriptions of the stress states in the rod and target, one may envision that substitutions could be made into the original three momentum and moment-of-momentum equations so that the original set of unknown variables (f, F, T, M, M_T, α, and η) would be replaced with the following six unknown variables: σ, β, σ_T, δ, α, and η (note that τ is not an additional unknown because the knowledge of σ completely defines it in terms of equation 15). Three additional definitive constraints are required to bring the number of equations in line with the unknowns. The problem transformation from expressions in force to expressions in stress facilitates the expression and justification of these constraints.

To understand, however, the rationale for these constraints, one must first understand how the moment of momentum equation 5 drives the ricochet solution down one of two primary paths, which the author terms "high-flux" and "low-flux" solutions. Each of these two paths brings a different set of forces into play. The term $x_f V\, dm/dt$ represents the moment about O that results from the momentum efflux of material as it exits the hinge (momentum entering the hinge has no moment because of how point O is defined). While the moment of the efflux can, in the theoretical sense, diminish to zero if the rod is, for example, without strength and ricochets at the striking angle (when $\alpha = \pi/2 - \theta$ at which point x_f approaches zero), the moment of the efflux is always non-negative and largely determined by the striking velocity V of the rod. All other terms in this equation are moments that derive from applied forces. While M_T can be positive or negative, depending on the skew of the target stress, the terms M and Tx_s are have been shown strictly non-negative, owing to the kinematics of material flow through the hinge.

When the momentum efflux is large, the resulting moment must be counterbalanced by the rod moment M and a positive target moment M_T. The presence of shear traction in the rod T actually works against the high-flux balance of moments, and thus hinders the formation of a ricochet hinge. On the other hand, when the momentum efflux is small, the problem approaches that of a quasi-static nature, and a natural balance must be established in which the rod moment M is countervailed by a negative target moment M_T and/or shearing moment Tx_s. It is not surprising, therefore, that the definitive constraints to be introduced will be different for high-flux and low-flux conditions. In the algorithmic implementation, the sign of the target moment M_T is used to differentiate the high-flux condition ($M_T > 0$) from the low-flux condition ($M_T \leq 0$).

2.5.1 High-Flux Constraints

The definitive high-flux constraints are as follows:

$$\text{High-Flux Constraint 1: } \sigma = Y, \tag{32}$$

$$\text{High-Flux Constraint 2: Either } \alpha = 0 \text{ or } \sigma_T = H, \tag{33}$$

and

$$\text{High-Flux Constraint 3: Either } \eta = 0 \text{ or } \delta = 0. \tag{34}$$

The first constraint reflects the observation that the presence of shear traction hinders the formation of a high-flux plastic hinge. It is thus assumed that τ will equal zero in the high-flux condition. And when $\tau = 0$, it follows directly that $\sigma = Y$.

The second constraint reflects the understanding that, for high-flux conditions, increasing σ_T and/or α will serve, respectively, to balance and/or mitigate the moment of momentum that results from the high rate of rod material flowing through the control volume. However, only the increase of σ_T serves that balance, while simultaneously minimizing the plastic work done on the deforming rod. Increasing α represents an increase in the overall plastic work rate, as the total turning of the rod that is continuously fed through the hinge is given by the angle $\pi/2 - \theta + \alpha$.

Thus, in achieving the required moment-of-momentum balance, the target will first attempt to employ a redistribution of elastic target stresses while retaining the $\alpha = 0$ condition that minimizes plastic work on the rod. Only when the target stress redistributions (in both magnitude and skew) are no longer able to, on their own, provide that balance (implying the target stress has reached its limiting value of $\sigma_T = H$) will the target attempt to achieve the balance through an increase in α. The second high-flux constraint captures this transitional behavior.

Note however, as α is increased, that the ricochet solution is still elastic from the perspective of the target because, while the target stress of the bearing surface may be at the level of imminent yield ($\sigma_T = H$), the area of the bearing surface is still less than the full elliptical footprint if the target stress is skewed (as defined by a nonzero value of δ). Were the target to be deforming plastically, the complete interaction ellipse would necessarily be engaged in the target. And this brings us to the third high-flux constraint, which defines the nature of plastic ricochet as possibly occurring only when the full interaction ellipse is engaged by the target. And thus, a ricochet solution is either elastic ($\eta = 0$) or else the full interaction ellipse is engaged ($\delta = 0$).

Note also that the target force line-of-action bounding constraint $|\eta| \leq \alpha$, discussed in the prior section of this report, guarantees that for a transition-to-target plasticity to occur ($\eta \neq 0$), there must already exist a level of rod rebound ($\alpha > 0$).

2.5.2 Low-Flux Constraints

The definitive low-flux constraints are as follows:

$$\text{Low-flux constraint 1:} \quad \alpha = 0, \tag{35}$$

$$\text{Low-flux constraint 2:} \quad \eta = 0, \tag{36}$$

and

$$\text{Low-flux constraint 3: either } \sigma = Y \text{ or } \delta = 0. \tag{37}$$

As mentioned in the discussion of the high-flux condition, increasing α represents an increase in the work performed in deforming the ricocheting rod. Its introduction in the high-flux solution was predicated on the inability of the target stress to produce enough moment about O to counter the moment produced by the $\alpha = 0$ momentum flux. In low-flux cases, however, the flux moment is, by definition, small. And so increasing α beyond zero does little to affect the moment balance (*i.e.*, its introduction is not necessary to achieve the moment balance, as in the high-flux case), but does so at the expense of increased plastic work on the rod. Thus, the first constraint reflects the intent to minimize the work performed on the ricocheting rod because it does not otherwise preclude a balance to the moment-of-momentum equation.

The second constraint follows immediately from the first, based on the prior developed target force line-of-action bounding constraint ($|\eta| \leq \alpha$).

The third constraint is not technically based, but reflects the realization that the current model, for low-flux solutions, cannot judiciously ascertain what proportion of counter-clockwise moment (about O) arises from shear stress in the rod vs. stress skewing in the target. The practical solution embodied in this constraint is that the counter-clockwise moment may arise from one source, or the other, but not both.

In light of this third constraint, the methodology attempts two solutions for these low-flux cases: one that solves for a negative M_T while holding T equal to zero (implying $\tau = 0$, and thus $\sigma = Y$); and the other that solves for a positive T while holding M_T equal to zero (implying σ_T uniformly distributed over the interaction footprint, and thus $\delta = 0$). If both approaches provide a viable ricochet solution, that which is seen to perform the smallest amount of elastic work on the target is adopted as the preferred ricochet solution. Since, for elastic deformation, the target displacement will be proportional to the elastic strain and thus proportional to the stress, the criterion for minimum work on target is that solution which minimizes $F \cdot \sigma_T$.

2.6 Ballistic Response Criteria

The ascertainment of a viable ricochet solution depends on the successful solution of equations 3–5, subject to the definitions, constraints, and assumptions inherent in the supporting equations that followed. Even so, a solution strategy is not plainly obvious because of the highly nonlinear nature of coupled equations, which are nonetheless algebraic in nature. It is not the intent of this report to lay out a flow chart of algorithmic details, but several comments are in order here with regard to putting ricochet in the larger ballistic context.

Whether or not a viable ricochet solution is found, there exists the possibility that an alternative nonpenetrating ballistic solution, involving dwell of the penetrator, may be likewise viable. While one could adopt an approach that, for example, looks to the respective target stress to gauge whether ricochet or dwell is more likely, the current model instead adopts the hypothesis that a ricochet solution is always preferable to a dwell solution because ricochet will involve less plastic work in bending the penetrator than dwell would in eroding it. In either event, the target stress must remain on the verge or below the target-resistance value of H in order to be a viable nonpenetrating solution.

There will also exist conditions when a high-flux, low-flux, or dwell solution is sought, but for which no viable nonpenetrating (ricochet or dwell) solution is found. In these cases, the appropriate conclusion is that the ballistic scenario proceeds as a penetration event.

3. Model Solutions

In this section, model results will be displayed that demonstrate the capacity of the model. In the results presented here, the Tresca yield criterion has been assumed for the penetrator material, such that $c = 0.5$ in equation 15.

One method of presentation that is very informative is a phase diagram of ballistic response, in which the predicted ballistic response is plotted on a two-dimensional graph that spans the engagement obliquity on one axis and another ballistic variable of interest on the other axis. The ballistic responses that one observes in these phase diagrams are given by the 2- or 3-letter designations described in table 1. These phases describe whether the ballistic engagement is predicted to result in penetration, dwell, or ricochet. If it results in ricochet, the ricochet mode is more precisely delineated in terms of rod response, target response, and momentum-flux mode. While the target-response and flux-mode designations are technically very specific, the rod-response designation is somewhat arbitrary and is meant to denote whether the stress-state in the rod may be primarily characterized by bending or compression. The arbitrary cutoff selected is that if the axial force in the rod exceeds 50% of the theoretical maximum value of f_{max}, then the rod's mode is denoted as "compressive." Otherwise, the mode is denoted as "bending." This 50% cutoff value, in the absence of shear traction, corresponds roughly to a value of β equal to 66°.

Table 1. Ballistic-response and ricochet mode designations.

Ballistic Response Modes:		
Pen.	penetration	
D	dwell (flow splitting)	
"*xyz*"	ricochet designation (as follows):	
***x* (rod response):**		
B	bending	$0 < f \le 0.5 \cdot f_{max}$ $(\beta > \sim 66°)$
C	compressive	$0.5 \cdot f_{max} < f < f_{max}$ $(\beta < \sim 66°)$
***y* (target response):**		
R	rigid	$\sigma_T < H,\ \alpha = 0,\ \eta = 0\ (\delta \ge 0)$
Y	at yield	$\sigma_T = H,\ \alpha \ge 0,\ \eta = 0\ (\delta \ge 0)$
P	plastic	$\sigma_T = H,\ \alpha > 0,\ \eta \ge 0\ (\delta = 0)$
***z* (flux mode):**		
(blank)	high-flux	$\tau = 0,\ M_T > 0$
*	low-flux 1	$\tau > 0,\ M_T = 0\ (\delta = 0)$
–	low-flux 2	$\tau = 0,\ M_T \le 0\ (\sigma = Y)$

Figure 8 shows, for example, the ballistic phase diagram as a function of target resistance and impact obliquity for the impact of a steel rod (ρ_R = 7800 kg/m^3) of strength 1 GPa, when impacting a target at 1000 m/s. The figure shows several trends including a critical engagement angle (to produce ricochet) that drops from ~85° to –50° as the target resistance is increased from 0.1 to 9 GPa. Beyond a resistance of 4.9 GPa, penetration is no longer possible as the rod either dwells upon or ricochets from the target surface.

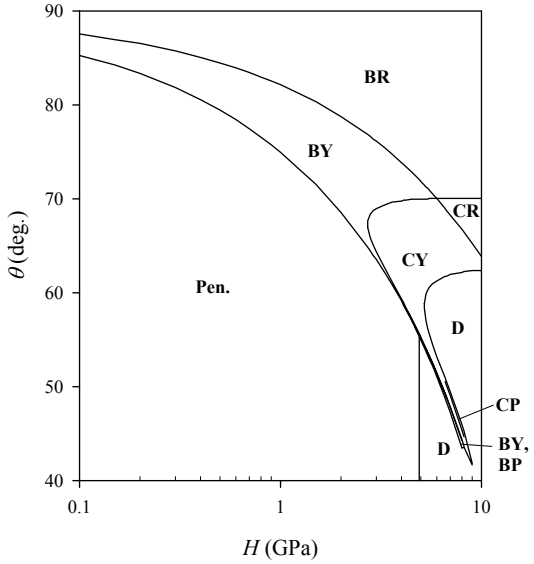

Figure 8. Phase diagram of ballistic response as a function of H and θ, for engagement where ρ_R = 7800 kg/m^3, Y = 1 GPa, and V = 1000 m/s.

In figure 9, the same rod density and impact velocity are examined, though this time with a fixed target resistance of 2 GPa, and with the variation in rod strength studied between limits of 0.01 and 10 GPa. The transition from penetration to ricochet is strongly cusped at a rod strength level of ~0.2 GPa. Above this rod strength, the target resistance H is the primary determinant of the ricochet threshold. However, on the low-Y side of the cusp, it is the rod's relative lack of strength that governs the shape of the ricochet curve, as it tries to penetrate in almost a liquid-jet-like manner. Because a rod's speed remains unchanged during ricochet, stagnation stresses do not play a role. And thus, from equations 11, 13, and 14, a strength-free rod is unable to exert axial force f or bending moment M toward balancing the momentum and moment-of-momentum equations.

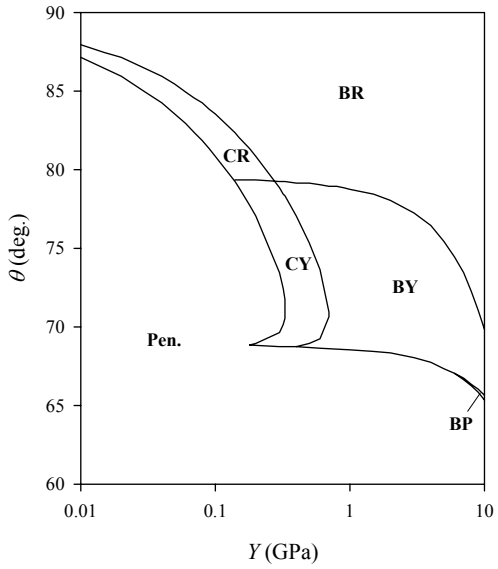

Figure 9. Phase diagram of ballistic response as a function of Y and θ, for engagement where $\rho_R = 7800$ kg/m^3, $H = 2$ GPa, and $V = 1000$ m/s.

In figure 10, a more complicated result (*i.e.*, with many ricochet response modes) is presented wherein the striking velocity V is varied for the impact of a hypothetical aluminum (Al) rod ($\rho_R = 2700$ kg/m^3) with strength $Y = 1.2$ GPa onto a target possessing a resistance of $H = 1.25$ GPa. Figures 10a, 10b, and 10c show, respectively, the rod response, target response, and flux mode of the ricochet solution, whereas figure 10d integrates these results onto a single graph. While it may seem unusual to predict ricochet at very small obliquities, for cases when the impact velocity is small, the experiments of Reid *et al.* (*5*) show exactly such ricochet behavior at impact obliquities of 10° and even for "normal" impacts. While Reid *et al.* called these results "buckling" rather than "ricochet," ricochet would tend to be a better description, as buckling, used in the traditional sense, would occur mid-length along the column. Their data, by contrast, clearly shows the rod deformation at the striking end of the rod, where one would expect a hinge to form. The residual curling of the rod tip they observe is likely an artifact of a residual-stress-induced moment as the rod material exits the hinge. Such residual moments are not addressed in the theory presented here, as the rod material is explicitly assumed stress-free as it exits the hinge. In any event, predictions of ricochet at small obliquity should not be a cause of undue modeling concern.

While the diagrams of figures 8–10 depict the ricochet, dwell, or penetration phases that are predicted by the model for various engagement conditions, more detailed data are also available from the model. Take the problem modeled in figure 10, for example, and confine the examination to a striking velocity of 700 m/s. For this striking velocity, figure 11 depicts many of the relevant ricochet variables as a function of the striking obliquity θ. Figure 11a depicts the

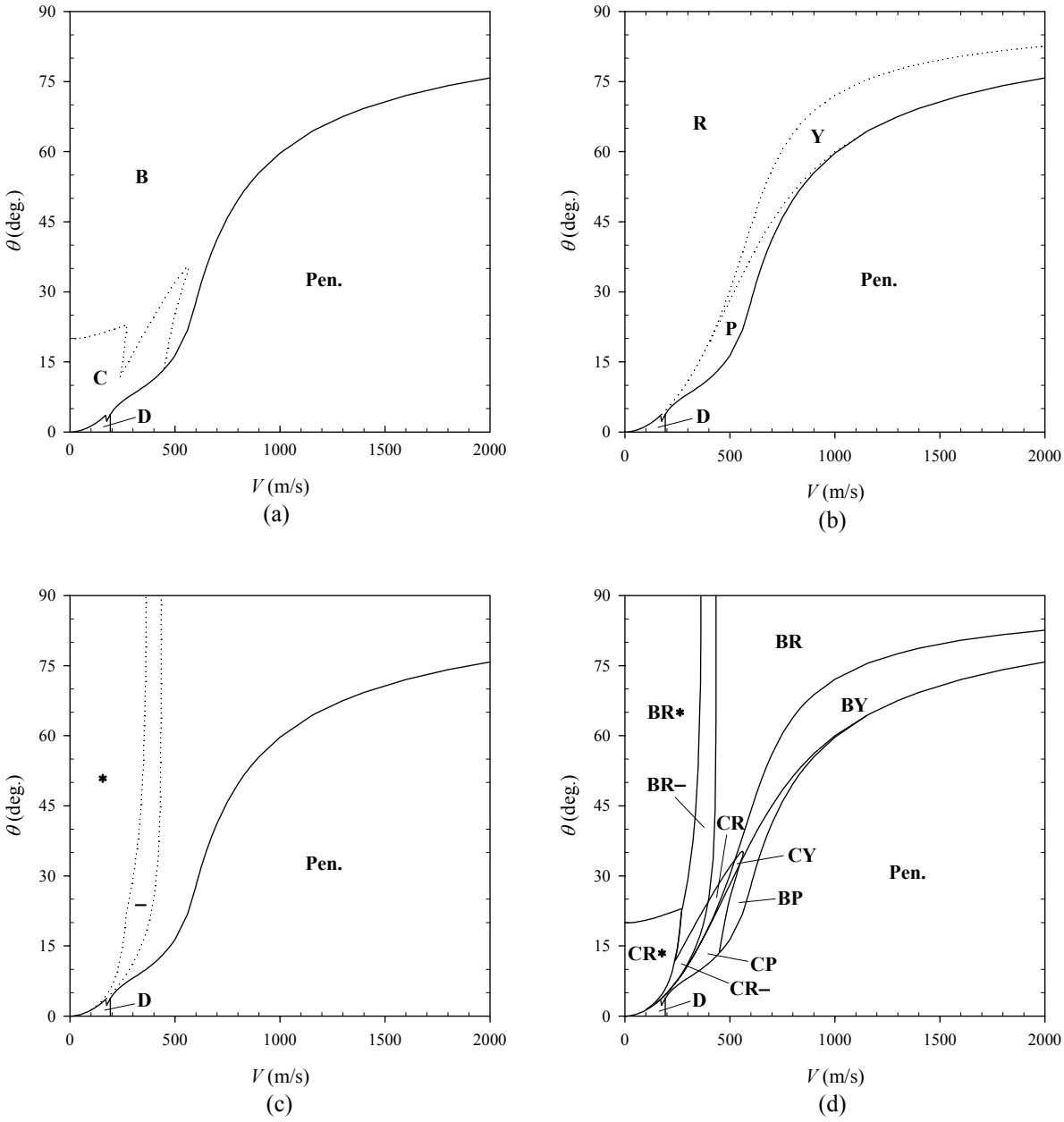

Figure 10. Phase diagram of ballistic response as a function of V and θ for engagement where $\rho_R = 2700$ kg/m^3, $Y = 1.2$ GPa, and $H = 1.25$ m/s. The figures depict (a) the rod response, (b) the target response, (c) the flux mode, and (d) integrated ricochet response.

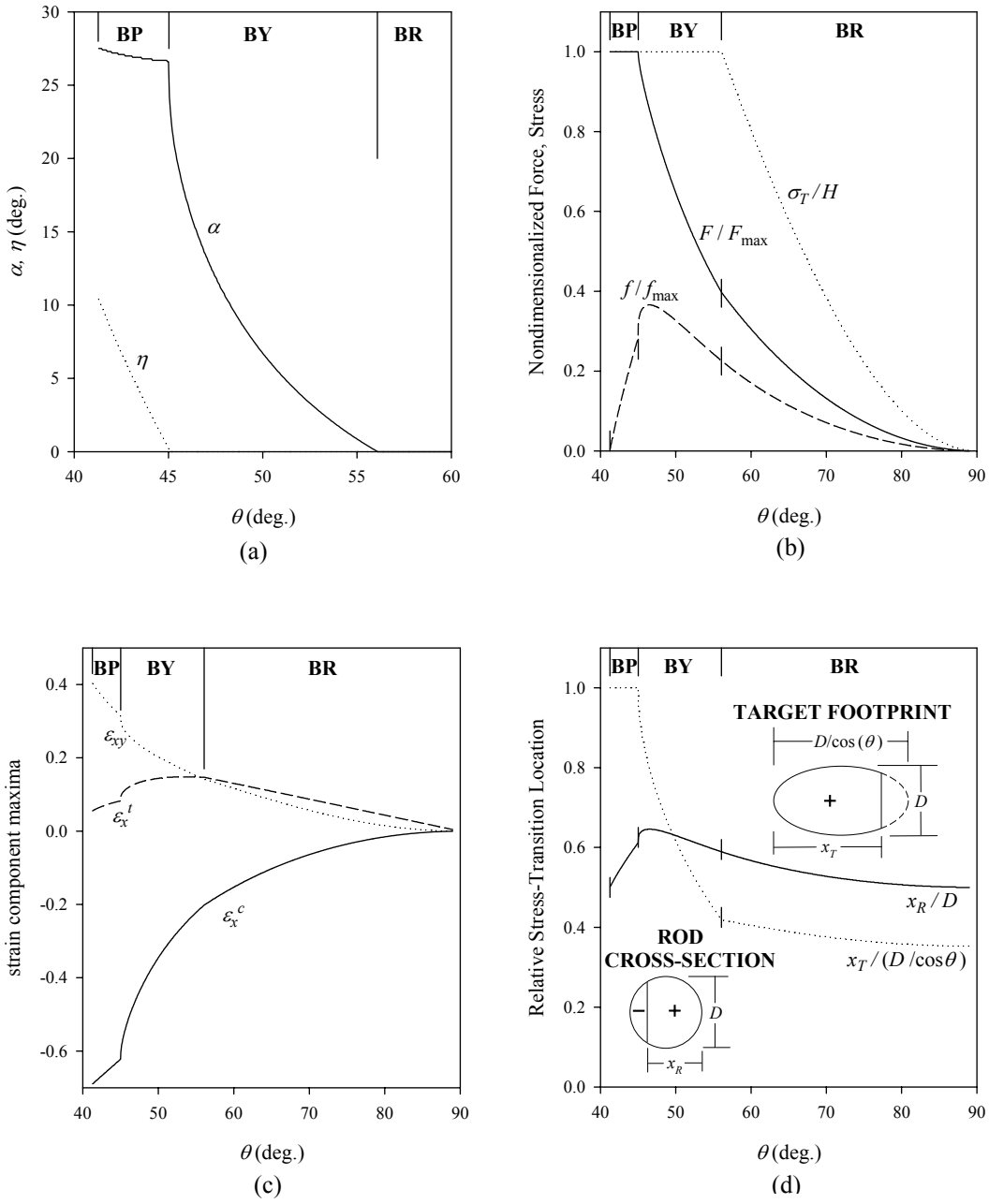

Figure 11. Ricochet variables as a function of θ for the case where $V = 700$ m/s, $\rho_R = 2700$ kg/m^3, $Y = 1.2$ GPa, and $H = 1.25$ m/s. The figures depict (a) ricochet and line-of-force angles, (b) target forces and stresses, (c) strains, and (d) locations of stress-transition.

angle of ricochet from the target surface, α, and the target force line-of-action angle, η. Figure 11b depicts the target force and stress, as well as the net rod force, all of which have been nondimensionalized by their limiting value. Figure 11c shows the strain component maxima that would result from the ricochet predictions and Figure 11d shows the stress-reversal location in the rod cross section (from tension "–" to compression "+") and the stress-truncation location in the target interaction ellipse (from compression "+" to stress-free " "). At the top of each of these figures are the letter designations BP, BY, and BR, denoting the respective regions of ricochet mode associated with the graph variables. The disparity between the target force, $F/F_{\max}$, and target stress, σ_T/H, curves is indicative of a target force that is not acting over the complete elliptical bearing surface [in fact, $(F/F_{\max})/(\sigma_T/H)$ represents the fractional area of the target's elliptical bearing surface that is subjected to σ_T].

4. Observations on Model Behavior

4.1 Ricochet-Mode Transition

Though the rationality of model response was not ensured during model development, the model was subsequently observed to transition smoothly from one ricochet mode to another. For example, in the transition from a yielding to a rigid target, the ricochet angle drops smoothly to zero (figure 11a). Likewise, on the verge from plastic to yielding ricochet, the line of target force action smoothly transitions towards $\eta = 0$. Figure 11b similarly shows continuous behavior in the target forces and stresses. However, a small dislocation is observed in the net rod force across the plastic-to-yielding transition. This dislocation in net rod force arises from a similar jump in x_R (figure 11d). Likewise, a jump in x_R will cause a dislocation in the rod strains, as well, as observed in figure 11c. The origins of such a dislocation are not immediately clear.

Another exception to smooth transition behavior is between the low-flux modes denoted "∗" and "–". The jagged response, seen in figure 10a, across the compressive vs. bending transition of the rod, is specifically attributable to the flux-mode transition from "∗" to "–". This jagged response is understandable from a modeling point of view, given the model's simplifying "either/or" assumption embodied in low-flux constraint 3. A truly accurate low-flux description would, without doubt, entail simultaneous elements of both rod shear and target moment, explicitly precluded by the low-flux constraint 3.

Fortunately, none of these transition dislocations has been observed to produce any aberrant dislocations in the ricochet vs. no-ricochet predictions, instead limiting themselves to dislocations in the predicted mode of ricochet or some of the model variables of ricochet.

4.2 Behavior of Strain

The use of strain calculation was cited earlier as a means of determining whether the ricocheting rod is likely to remain an intact rod or break into a spray of deflected fragments. The possibility of either of these results was empirically demonstrated very clearly by Jonas and Zukas (*2*) wherein rod fracture during a ricochet event could be brought on with a slight increase in striking velocity. Their observation is compatible with the current model behavior, which shows the ricochet angle α increasing with increasing striking velocity (all other things equal, once the target reaches the yield condition). Plastic strain, in turn, increases with increasing α, and so likewise the propensity for rod failure during ricochet increases with striking velocity. Even in the absence of an increasing α (*i.e.*, when the target is rigid and α remains zero), the maximum strain in the rod increases with increasing striking velocity because of a shift in location of the neutral bending fiber of the rod.

4.3 Influence of Rod Aspect (*L*/*D*)

In Tate's ricochet model (*3*), rod aspect is explicitly tied in to the prediction of ricochet because the model posits that, for ricochet to occur, the rigid body constituting the rod must rotate away from a penetrating orientation. The longer the rod length (for a fixed rod diameter), the more difficult this task becomes, as the more rotational inertia must be overcome in that rotation process. By contrast, the current model carries no explicit influence of rod length or aspect. This absence comes from the assumptions adopted by the model that govern the nature of ricochet. In particular, the current model calculates the ability to sustain ricochet in a steady-state capacity (by way of a plastic hinge), and in that sense the model applies to rods of arbitrarily large length.

In reality, ricochet is likely a combination of these behaviors. While a hinge may be trying to establish itself in the moments following the oblique impact of a rod upon target (current model assumption), simultaneously there are bending moments and shear forces working to rotate the rod away from a penetrating orientation (the Tate assumption). It seems likely that as rod aspect (L/D) becomes large, assumptions akin to those in the current modeling must prevail, whereas the opposite seems likely for rods of low aspect (where rod rotation becomes easier than plastic-hinge formation). If this is the case, then there exists an intermediate range of rod aspect ratios where neither of the two approaches wholly suffices.

While no constructive solution is offered here to address (or even define) this intermediate range of rod aspect ratios, it should be obvious that it is never harder to ricochet a finite length rod compared to its arbitrarily long counterpart. And in that sense, the predictions of the current model should represent a conservative estimate of the ricochet threshold.

4.4 Nose-Shape Effects

It has already been mentioned how the nose shape of a rod can play a key role in ricochet. A conical nose, for example, while conducive to good aerodynamics, is more prone to ricochet than

a flat-nosed projectile, which can "bite" into the target surface more readily. Already mentioned is how the current model's methodology does not treat those initial moments following impact, where deforming rod-nose geometry is a key influence. Rather, the current model attempts to answer the question, should ricochet be initially established, of whether the rod and target stresses can maintain this condition indefinitely. By contrast, models like those of Tate (*3*) and Rosenberg *et al.* (*8*) account for a nose-shape effect, but only for the very specific case of a square cross-section rod with a flat nose.

For cases with a hard target material (relative to the rod), the ability for the rod nose to "bite" into the target is minimized. Thus, differentiation in rod response as a function of nose shape is perhaps lessened as a result. But for engagements with hard rods (relative to target), the influence of nose shape must remain a significant one, and the current sustained-ricochet analysis will not substitute for appropriate analysis of nose-shape influence.

4.5 Interaction Footprint Influence

One of the assumptions comprising the current ricochet model is the size of the interaction footprint where rod and target material physically interact. In the model, this zone is defined as an elliptical area formed by the projection of the rod's cross section, along the rod's trajectory, onto the target surface. For a rigid-target ricochet scenario, this interaction zone definition seems logical and appropriate, as it defines all the points on the target's surface that are in the direct path of oncoming rod material.

However, the situation becomes murkier for the case of ricochet when the target no longer remains rigid. In the model, the possibility of a gouged bearing surface between rod and target is allowed for, yet the specified size of the interaction footprint remains unchanged. In reality, and especially for softer targets (*e.g.*, Al), the target gouge that can accompany a ricochet can be quite significantly larger than this envisioned interaction footprint. The effect of permitting a larger interaction footprint in the model is that some engagement conditions, for which ricochet would previously have been precluded, are now capable of it. This premise was successfully play-tested in the model, though results are not presented because no rational scheme has yet been developed to suggest how large the interaction footprint might logically be extended, and under what conditions.

5. Simplified Model With Closed-Form Solution

One of the primary drawbacks of the model, as described, is the inability to present the critical obliquity for ricochet in terms of a closed-form solution. A remedy is sought to this deficiency, through a judicious application of simplifying assumptions to the model. While not capturing the complete nuance of the full model, the intent here is for the simplified model to, nonetheless, capture the essence of the phenomenology intrinsic to plastic-hinge ricochet.

Examine the three founding equations to the model (*i.e.*, equations 3–5). Equation 3 is constrained by the resistance of the target, H, which limits the allowable magnitude of the target-interaction force, F. Equation 4 is constrained by the requirement that the net axial rod force f be compressive (> 0), while at the same time being limited in magnitude to a force governed by the rod strength Y. However, the nature of the plastic hinge is that all particles in the rod, as they enter hinge, will be in a state of yield. The net magnitude of force f is therefore not determined by the stress state in the hinge (which is always yielding), but rather by the location of the so-called neutral fiber, which divides the compressively yielding side of the rod's cross-section from the side that is yielding in tension. In the typical case, f is primarily a driven, rather than a driving, quantity. However, there are exceptional cases where Y is so small that it cannot support the magnitude at which f otherwise needs to be driven to sustain ricochet. For example, the low-Y solutions depicted in figure 9 show a sharp change in behavior below the cusp at $Y = 0.18$ GPa. The behavior in this domain is driven by the allowable magnitude of f.

Equation 5, the moment equation, is perhaps the weakest link of the three equations. Admittedly, the force equations must make certain assumptions about the size of the interaction footprint in order to link the material strengths to the permissible forces f and F. However, the moment equation, in addition to these same assumptions, must also assume the stress distribution within that interaction footprint as well as the plastic-hinge geometry. If a simplified treatment were to discard one of the governing relations, therefore, the moment equation would make the best candidate. It is this approach that is adopted for the simplified solution.

Still, the number of unknowns needs to be significantly reduced in order to solve the equations. The easiest first step is to assume that the shear traction T is identically zero because its introduction into the general model was predicated on the need to provide a moment balance for certain low-flux cases. With the moment balance eliminated, the need for T is readily dispensed with. Next, judging from the relatively small contribution that target-gouging ricochet had in the solved examples described for the full model (not to imply that gouging ricochet is not a significant possibility in reality, but rather that it didn't appear to manifest greatly in the model), elastic-target ricochet would be a reasonable simplifying assumption, implying $\eta = 0$. A simplification that is harder to justify (which is nonetheless adopted) is that there is no rebound of the rod from the target surface following ricochet, such that $\alpha = 0$.

With these assumptions, the force equations 3 and 4 may be solved independently and the results combined simply. First consider the target-force equation 3, under the simplifying assumptions $T = \alpha = \eta = 0$:

$$F \tan\theta = V\dot{m} \,. \tag{38}$$

The upper-limiting target-force value, F_{max}, at the point of incipient yield is known from equation 17, while equation 6 defines the axial momentum flux rate in the rod. Applying the constraint $F_{max} \geq F$, for the case where $\eta = 0$, it may thus be deduced from equation 38 that

$$\frac{\sin\theta}{\cos^2\theta} \geq \frac{\rho_R V^2}{H} . \tag{39}$$

The positive-θ solution to equation 39 is

$$\sin\theta_{\mathrm{CRIT}(F)} \geq -\frac{H}{2\rho_R V^2} + \sqrt{1+\left(\frac{H}{2\rho_R V^2}\right)^2} . \tag{40}$$

This is the criterion, under the simplifying assumptions, that will guarantee that the target's resistance is not exceeded in achieving a ricochet.

On the other hand, it must simultaneously be guaranteed that the net rod force f remains between the bounds 0 to $f_{\max}$. Consider then, the rod-force equation 4, also under the simplifying assumptions $T = \alpha = \eta = 0$:

$$f\sin\theta = V\dot{m}(1-\sin\theta) . \tag{41}$$

For the lower constraint, $f \geq 0$, equation 41 would indicate that $\theta_{\mathrm{CRIT}(f)} \leq 90°$. This result merely indicates that a negative f is not even possible under the simplifying assumptions. For the upper constraint $f_{\max} \geq f$, it may be deduced from equation 41, with the use of equations 6 and 11, that

$$\sin\theta_{\mathrm{CRIT}(f)} \geq \left(1+\frac{Y}{\rho_R V^2}\right)^{-1} . \tag{42}$$

This is the criterion, under the simplifying assumptions, that will guarantee that the compressive force in the rod does not exceed the permissible limit in achieving a ricochet. However, both equations 40 and 42 must simultaneously be satisfied in order to facilitate ricochet. Fortunately, the merging of these two criteria is trivially straightforward, to yield the simple ricochet model as simple model:

$$\sin\theta_{\mathrm{CRIT}} \geq \max\left[-\frac{H}{2\rho_R V^2} + \sqrt{1+\left(\frac{H}{2\rho_R V^2}\right)^2} \;,\; \left(1+\frac{Y}{\rho_R V^2}\right)^{-1}\right]. \tag{43}$$

While equation 43 achieves only a semblance of the full ricochet model, it does so in a single closed-form equation that is much more comparable in spirit to the Tate or Rosenberg model forms. To see how this model compares to the full model, the engagements analyzed with the full model by way of figures 8–10 are shown in comparison to the simple model in figure 12. It is observed that, for the most part, the simple model trends closely to the full model's predictions. Those regions where the full model shows a greater propensity to ricochet arise from relaxations on the constraint, which characterizes the simple model, $\alpha = \eta = 0$. Conversely, those regions where the full model has a lesser propensity to ricochet vis-à-vis the simple model

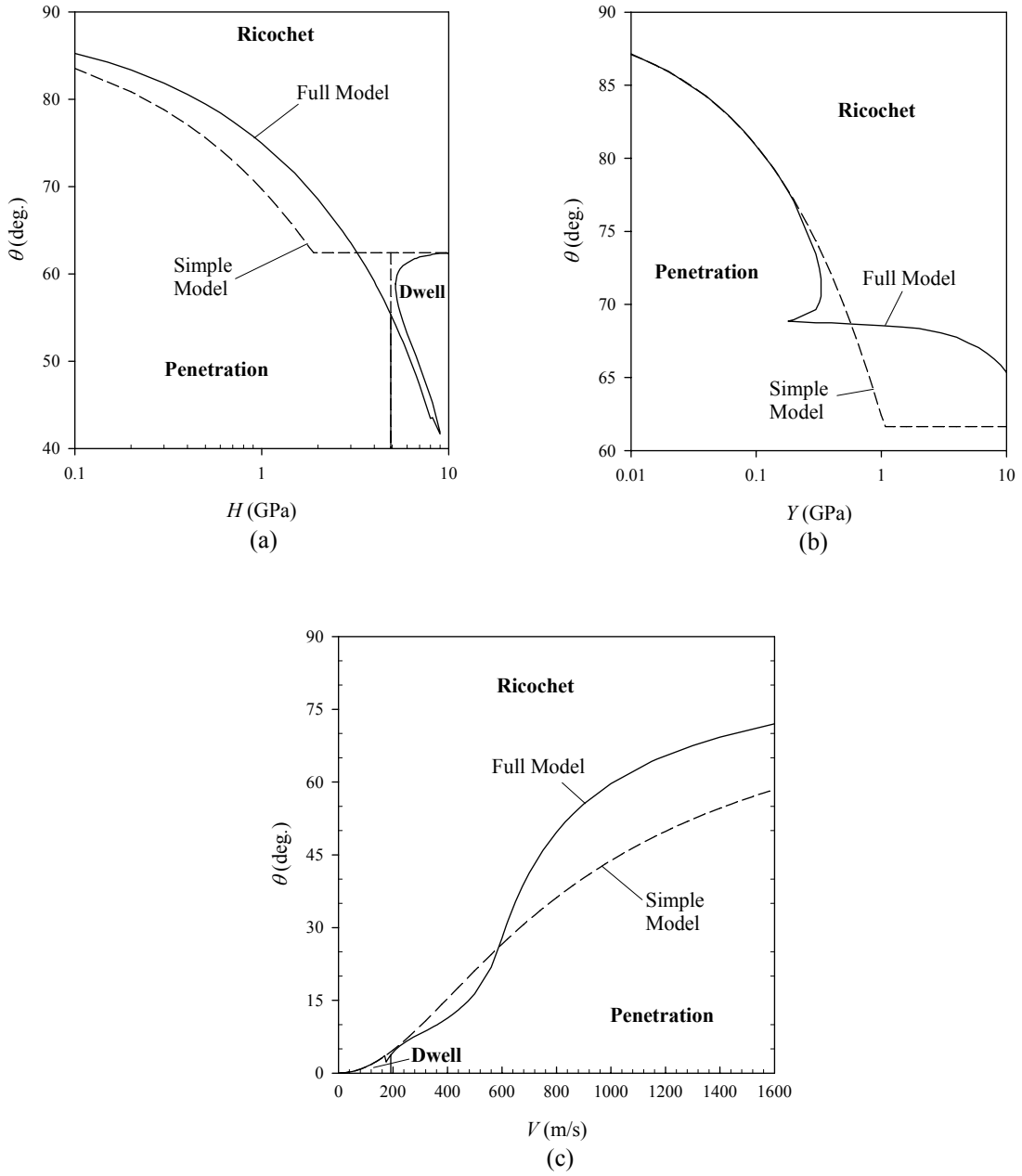

Figure 12. Comparison of full ricochet model to the simple model for prior cases where (a) H is varied, (b) Y is varied, and (c) V is varied.

arise from the added constraint that the moment equation puts upon the target stress field, which is not factored into the simple model.

One final note is that, even with the simple form of the model, the strain calculations in the plastic hinge may proceed according to the established methodology. In particular, the kinematic relations given by equations 9 and 10 may be applied to obtain s_1 and s_2, respectively, all the while incorporating the $\alpha = 0$ assumption inherent to the simple model. The net rod force f may

be evaluated from the simplified version of equation 4, and β may then be back-calculated from equation 13. With β calculated, the rod's neutral fiber embodied in the variable x_R may be obtained from equation 12. Armed with s_1, s_2, and x_R, the strain relations delineated in equations 21–28 may be applied as before to evaluate the strain, using the result to evaluate the likelihood of a ricocheting rod retaining its integrity or, alternately, fracturing into pieces.

6. Comparison to Other Models

It is useful to know how the current model compares to, for example, the Tate (*3*) and Rosenberg (*8*) ricochet models. Already mentioned was the fact that neither of these other models is able to predict ricochet for engagement conditions that would otherwise meet the criterion of rigid-body penetration. Beyond this distinction, however, it is still illuminating to compare behaviors in other ballistic regimes, as well.

Thus, the engagements analyzed with the full model by way of figures 8–10 are shown in comparison to the Tate model in figure 13, and in comparison to the Rosenberg model in figure 14. Note that, in addition to the model parameters used by the current model, the Rosenberg model additionally requires the target density, while the Tate model additionally requires both the target density and the rod's aspect ratio (L/D). Thus, in the comparisons, the Tate and Rosenberg models are run against targets of density nominally that of both steel (7800 kg/m^3) and Al (2700 kg/m^3). Additionally, the Tate model results are calculated against rods of two aspect ratios $L/D = 10$ and $L/D = 30$, respectively.

For the engagements depicted in figures 13a and 14a, in which the target resistance H is varied as a model parameter, the Rosenberg model and the current model actually track in relative concert. The Tate model is less sensitive to changes in H, as such changes affect not the interaction force magnitude (which is given by Y), but only that force's line of action, via changes in the U/V ratio.

For the engagements depicted in figures 13b and 14b, in which the target resistance Y is varied as a model parameter, the Rosenberg model no longer closely tracks the current model. At low values of Y, where it was earlier observed for the current model that ricochet is driven by Y, it is the Tate model that somewhat follows the trend of the current model. For values of Y immediately beyond the cusp in the current model's treatment (where ricochet was earlier observed to be driven by H), the Rosenberg model is observed to briefly track the current model predictions. However, as rod strength Y is further increased, both the Tate and Rosenberg models diverge strongly from the current ricochet prediction, as conditions conducive to rigid-body penetration are approached. When conditions are actually met that would otherwise (*i.e.*, in the absence of target obliquity) permit rigid-body penetration ($Y \geq 3.35$ GPa against Al

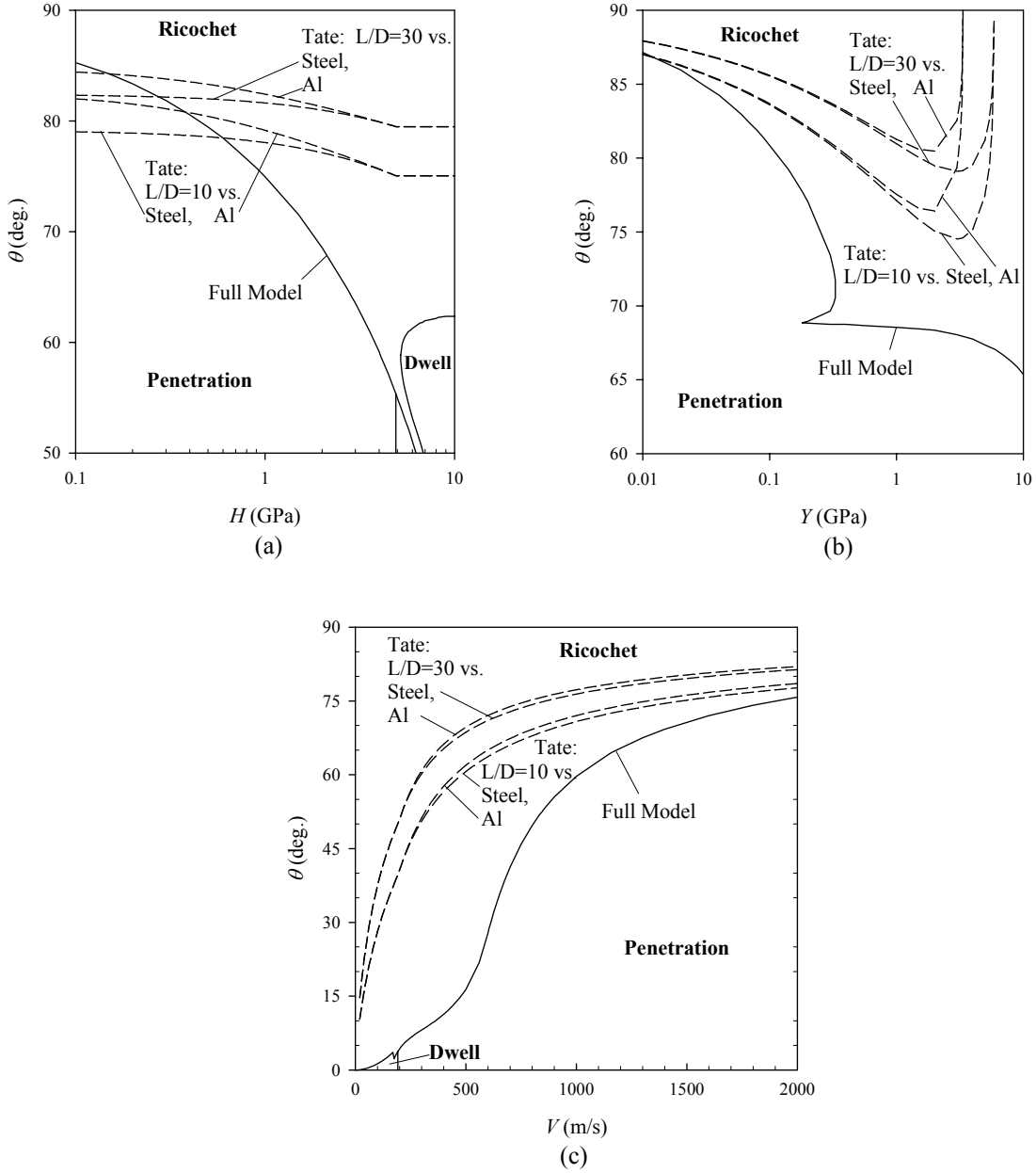

Figure 13. Comparison of full ricochet model to the Tate model (*3*) for prior cases where (a) H is varied, (b) Y is varied, and (c) V is varied.

and $Y \geq 5.9$ GPa against steel), neither the Tate nor Rosenberg models are able to predict viable ricochet.

For the engagements depicted in figures 13c and 14c, it is the striking velocity V that is varied as a model parameter. While the same basic trend is exhibited by all the models (that of increasing the critical ricochet angle with increasing striking velocity), there are significant disparities in the

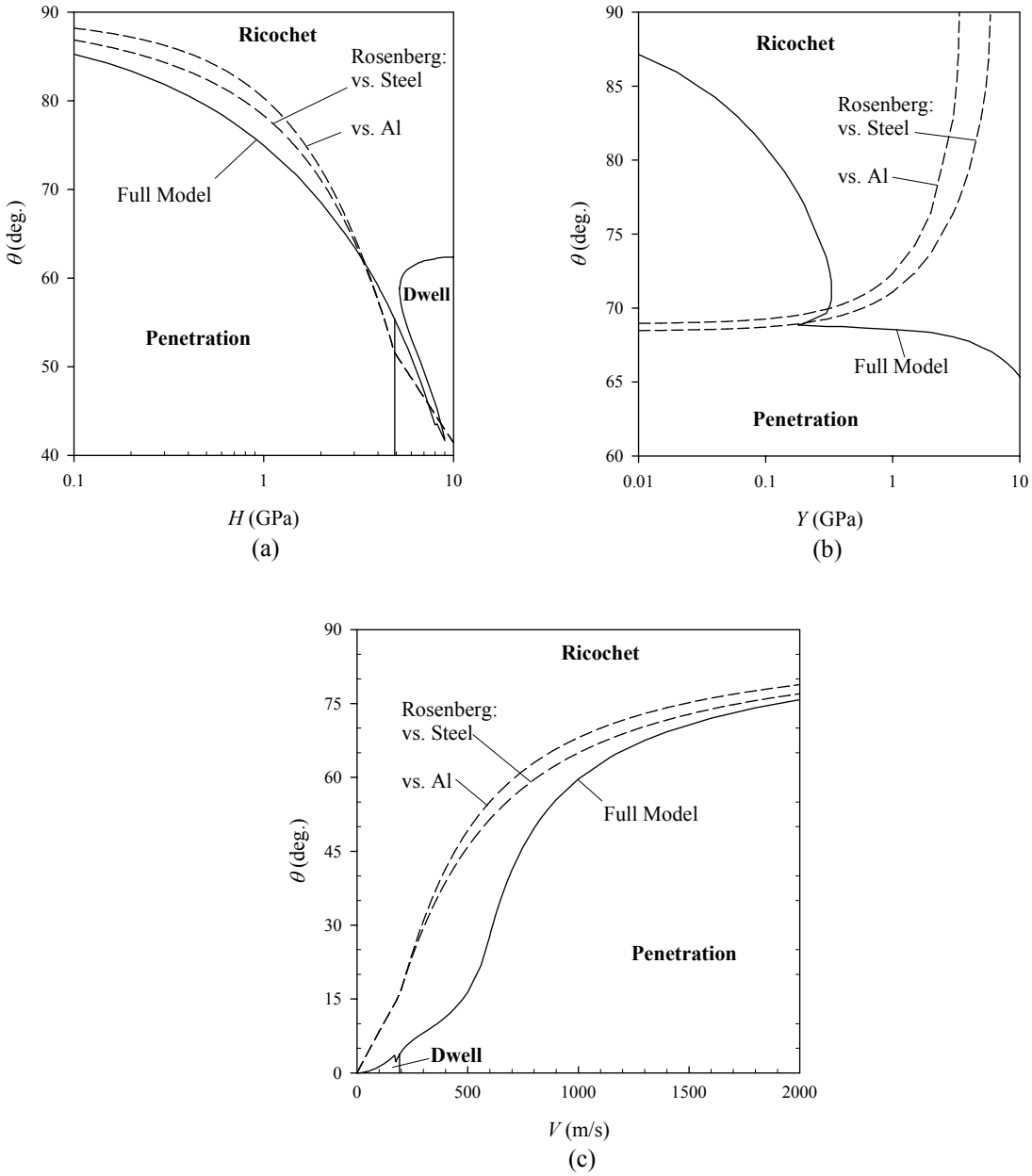

Figure 14. Comparison of full ricochet model to the Rosenberg model (*8*) for prior cases where (a) H is varied, (b) Y is varied, and (c) V is varied.

magnitude of the critical ricochet angle, especially as the striking velocity is decreased below 1000 m/s. For example, at a 500-m/s striking velocity, the current model predicts ricochet for engagements at ~16° obliquity, whereas the Rosenberg model, if applied to a hypothetical Al target ($\rho = 2700$ g/cm^3, $H = 1.25$ GPa) would require triple the obliquity, namely 49°, in order to achieve ricochet. The disparity with the Tate model is even greater at that striking velocity, with

critical ricochet obliquities above 60°, for rods of $L/D = 10$ or greater, against targets over the density range from Al to steel.

In general, it would appear that the current model shows a greater propensity to ricochet than either the Tate (*3*) or Rosenberg (*8*) models, most especially the Tate model. However, there are a number of regimes studied in which the current model behaves in many ways as the simpler Rosenberg model.

7. Comparison to Data

In the course of this investigation, several experimental studies were undertaken to probe the realm of ricochet. The results are presented here, and compared with the current ricochet model in both the full and simple forms, as well as with the models of Tate (*3*) and Rosenberg *et al.* (*8*).

In one study, 14.5-mm caliber B32 penetrators were shot against 1.75-in-thick (nominal) Al of Brinell hardness (BHN) 110, at various obliquities. The B32 is an armor-piercing projectile, weighing 63.5 g, consisting of a 53 mm, 41 g hardened steel (Rockwell C 65) core surrounded by a brass jacket. In a related study of B32 penetration (*14*), this projectile was successfully characterized as a cylindrical homogeneous steel penetrator ($\rho = 7850$ kg/m^3), 66.5 mm long × 12.45 mm diameter, with a yield strength Y of 4.46 GPa. That characterization has been retained for the current study on ricochet. The BHN 110 Al target is characterized with a resistance
$H = 2.03$ GPa, in accordance with Tate's formulation:

$$H = \sigma\left[\frac{2}{3} + \ln\left(\frac{2E}{3\sigma}\right)\right], \tag{44}$$

where $E = 75$ GPa, and $\sigma = \sigma_{ULT} = 0.363$ GPa. Owing to the pointed tip of the rigidly penetrating B32 projectile, a target shape factor of $k_T = 0.15$ was adopted in the associated penetration calculation (*14*).

The results of the 12 tests are described in table 2, while the data and associated predictions are shown in figure 15. The solid curved line is a prediction of the dividing line between partial penetration and perforation of the target plate, using a penetration model (*14*, *15*) that is unrelated to the ricochet predictions. It accurately separates the perforation data from the partial-penetration data. The full-model prediction is shown as a dotted line, while the simple-model prediction is shown with a dashed line. For striking velocities in the vicinity of 600 m/s, either form of the current model accurately predicts the dividing line between ricochet and penetration. However, at the 1000-m/s striking velocity, the data were more prone to ricochet than indicated by the model, with a disparity of ~15° between the full-model prediction (67.5°) and the actual (~52.5°) critical ricochet obliquity, θ_{CRIT}. Interestingly, the simple model

Table 2. Experimental result for B32 test series.

V_s (m/s)	θ (deg)	Result
1019	0	Perforation, V_r not obtained
999	0	Perforation, V_r = 815 m/s
991	30	Perforation, V_r = 726 m/s
538	30	Partial penetration
583	45	Ricochet
1004	45	Perforation, V_r = 543 m/s*
1003	50	Perforation, V_r = 561 m/s*
596	50	Ricochet
1005	55	Ricochet
619	55	Ricochet
595	60	Ricochet
999	60	Ricochet

Notes: *Projectile core fractured. V_r obtained via momentum average of residual-fragment velocities.

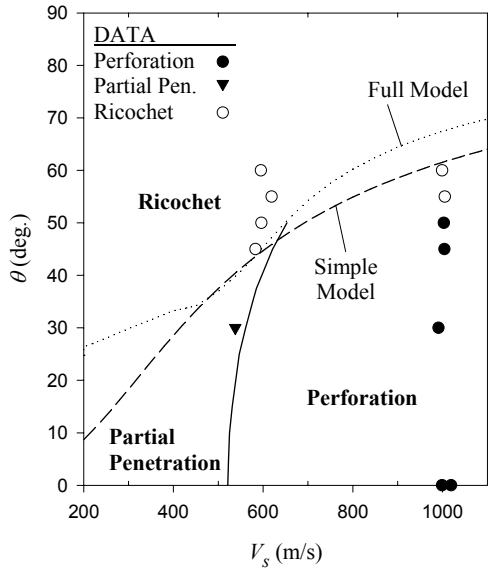

Figure 15. Results of B32 ricochet testing with comparison to ricochet/penetration predictions.

prediction, at 61.5°, fell closest to the data, within 10° of the actual critical ricochet obliquity at that striking velocity. Possible reasons for the disparity might include some or all of the aforementioned ideas, including short rod aspect ratio, interaction footprint size for hard rods on soft targets, as well as nose-shape effects for a rod that is anything but flat-nosed.

By comparison, the Tate and Rosenberg models predict no ricochet for any of these engagements, because of the rigid-rod nature of the ballistic engagement (*i.e.*, when U equals V, $\theta_{CRIT} \rightarrow 90°$ in these models). Therefore, despite the current model's disparity noted with respect to the data at 1000 m/s, the results are actually quite encouraging.

In a second study, 65 g, $L/D = 15$ tungsten alloy (WA) rods were shot against 2-in-thick (nominal) Al (BHN 190), at various obliquities. These hardened rods (Rockwell C 35.5) had hemispherical noses and were of dimension 102.3 × 6.81 mm. Their composition was 93% W, 4.9% Ni, and 2.1% Fe. In the modeling, the rod has a density of 17600 kg/m^3 and a strength of $Y = 1.1$ GPa. The BHN 190 Al target ($\rho = 2700$ kg/m^3, $E = 75$ GPa, and $\sigma_{ULT} = 0.627$ GPa) is modeled with a target resistance of 3.16 GPa, in accordance with equation 44. A total of 12 tests were conducted in this phase of the ricochet study.

The test results are given in table 3, while the data and model predictions are shown in figure 16. The curve dividing the "partial penetration" and "perforation" domains was predicted by a penetration model of the events (*14*, *15*). For those data which did not exhibit ricochet, this dividing line prediction accurately characterized all the ballistic data. The full model for ricochet was used to generate the curve that separates the "ricochet" domain from the others. The actual

Table 3. Experimental result for $L/D = 15$ tungsten-rod test series.

V_s (m/s)	θ (deg)	Result
691	35	Partial penetration + ricochet*
628	25	Partial penetration
1198	50	Perforation, $V_r = 986$ m/s†
1293	70	Partial penetration
907	40	Perforation, $V_r = 255$ m/s†
1402	70	Perforation, $V_r = 893$ m/s†
937	50	Ricochet
1079	55	Ricochet*
686	15	Partial penetration
1295	65	Perforation, $V_r = 812$ m/s†
836	20	Perforation
1088	65	Ricochet

Notes: *Ricochet resulted from rod delving into target and later reemerging out front surface.

†Projectile core fractured. V_r denotes largest velocity among the residual-fragments.

data show a significantly greater propensity to ricochet than predicted by the model. There are three ricochet data in the 900–1100 m/s striking velocity range that ricocheted at striking obliquities 10–20° less oblique than the model predicted, with critical ricochet angles as low as 50°.

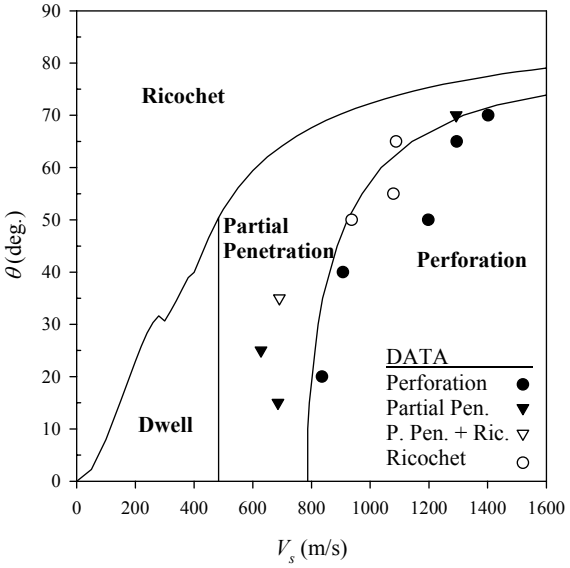

Figure 16. Results of $L/D = 15$ WA rod tests with comparison to ricochet/penetration predictions from the full-model currently proposed.

Further, there is one low-obliquity (35°) test at 691-m/s striking velocity, in which the impacting rod apparently fractured early in the penetration such that one segment of the rod penetrated the target partially and embedded itself, while the other segment reemerged through the target surface after penetrating in a submerged manner (all the while turning its trajectory). This test result is characterized in figure 16 as "partial penetration + ricochet." Likewise the ricochet datum at 1079 m/s and 55° obliquity also penetrated the target in a submerged manner prior to reemerging through the front of the target surface. This datum is one that had been predicted to perforate the target.

These "delving" ricochets, as they might be called, are clearly operating under a different ricochet phenomenology than the plastic-hinge approach put forward in the current model. Most likely, for these delving ricochets, the surface interaction, while not producing ricochet directly, introduces a large yaw as the rod begins to delve below the target surface. The flow pattern around the highly yawed projectile likely introduces a significant lateral force that continuously pushes the rod tip away from its local trajectory. The net effect is a delving ricochet, in which the rod takes an arcuate trajectory beneath the surface of the target, before reemerging from the front surface.

Even the ricochet data that did not manifest as delving ricochets operated a bit outside of the phenomenology proposed in the current ricochet model. Namely, the gouges associated with the plastic ricochets at 937- and 1088-m/s striking velocity were much larger than the interaction footprint proposed in the model. For the 50 and 65° obliquity at which these two tests were

respectively conducted, the interaction footprint should have been 10.6 and 16.1 mm in respective length, while in fact, the experimental record records the gouge lengths as 119 and 111 mm long, respectively. Now, it cannot necessarily be supposed that the instantaneous interaction footprint in these experiments was an order of magnitude larger than hypothesized by the model. An equally, perhaps, more plausible possibility is that a smaller interaction footprint rode itself along the target surface over time, as the trajectory of the rod changed under the forces and moments to which it was subjected. Such a sliding footprint would leave a residual gouge for the post-test examination that is larger than the instantaneous interaction footprint.

In any event, there is a disparity noted, not only between the predicted and actual critical ricochet angles, but also in the ricochet phenomenologies proposed by the model vis-à-vis those noted experimentally, including delving ricochet and extended ricochet gouges, not accounted for in the model. Anecdotal experience suggests that the delving-ricochet phenomenon is far more prevalent in Al, soil and other soft targets than, for example, in steel targets. Despite these noted shortcomings, a comparison of the model to the existing Tate and Rosenberg models shows the current model on a footing closest to the experimental reality. Figure 17 shows that comparison between the full model and the various other ricochet models, including the simple, Tate and Rosenberg models. In many regards, the current model follows the trend of the Rosenberg model. However, the current model is seen to track closer to the data than the other models, especially at the higher velocities. As before with the B32 tests, the simple model for ricochet tracks closest of all to the ricochet data, though just by a slight margin compared with the full model.

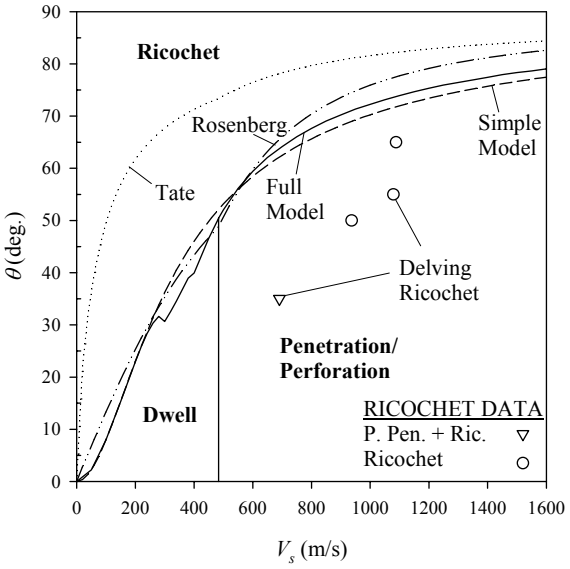

Figure 17. Comparison of model predictions for the current ricochet model (both full and simple forms), the Tate as well as the Rosenberg models against the results of L/D = 15-WA rod tests.

8. Conclusions

A rod-ricochet model has been proposed, based upon the premise that ricochet occurs by way of a plastic hinge in the rod, located at and stationary with respect to the target interface, into which the moving rod feeds itself. Unlike the Tate ricochet model (*3*), which gauges whether initial interaction forces are sufficient to rotate the rod as a rigid body from the target interface, or the Rosenberg model (*8*) which examines whether the forces from the rod-tip interaction are sufficient to deflect the tip from a penetrating trajectory, the current model bases its ricochet judgment on the answer to a different question: Can the interaction stresses and fluxes in the rod and target produce the forces and moments required to continuously sustain a plastic hinge at the rod/target interface?

While analytically based, the full model proposed here cannot be distilled down to a single inequality, as in the case of the models of Tate or Rosenberg *et al.* One reason is that, in the full model currently proposed, the prediction of ricochet feasibility is not prescribed as a mere constraint on rod strength or target resistance. Rather, a multiplicity of requirements involving dynamic force and moment equilibrium as well as kinematic constraints must be simultaneously satisfied for each and every considered configuration. Despite these added complexities in the modeling premise, the model is still represented by a handful of algebraic equations that must be simultaneously solved.

Nonetheless, a simple version of the full ricochet model was also developed, which satisfies the core force relations of the full model while dispensing with the moment relation and simplifying the constraints. Like the Tate and Rosenberg models, this simple version of the current ricochet model is expressible in terms of a single closed-form inequality relation.

Oblique-impact testing spanning the ricochet threshold was conducted for two separate ballistic threats, including the B32 14.5-mm bullet, as well as an L/D = 15-W rod. In general, the data from the 24 tests showed a greater propensity to ricochet than predicted by any of the models examined. However, the current model in its simple form proved the best predictor of ricochet, in comparison to the full model, the Tate ricochet model and the Rosenberg model.

Possible reasons for the disparity between model and data were discussed, including aspect ratio and nose-shape effects of the rod, as well as the assumed size of the interaction footprint between rod and target. Additionally, some of the experimental data witnessed a delving ricochet, in which the rod reemerged from front surface of the target, following an arcuate trajectory beneath the surface of the Al target. Such ricochets would seem to fall outside the realm of plastic-hinge phenomenology described in the current model. Despite these disparities however, the overall trend of the model was in line with the experimental data, and with an apparent improvement over the earlier models cited.

9. References

1. Goldsmith, W. Non-Ideal Projectile Impact on Targets. *Ricochet. Int. J. Impact Engng.* **1999**, *22* (10), 95–395.

2. Jonas, G. H.; Zukas, J. A. Mechanics of Penetration: Analysis and Experiment. *Int. J. Engng. Sci.* **1978**, *16*, 879–903.

3. Tate, A. A Simple Estimate of the Minimum Target Obliquity Required for the Ricochet of a High Speed Long Rod Projectile. *J. Phys. D: Appl. Phys.* **1979**, *12*, 1825–1829.

4. Senf, H.; Rothenhaeusler, H.; Scharpf, F.; Poth, A.; Pfang, W. Experimental and Numerical Investigation of the Ricocheting of Projectiles From Metallic Surfaces. *Proceedings of the 6th International Symposium on Ballistics*, Orlando, FL, **1981**.

5. Reid, S. R.; Edmunds, A. J.; Johnson, W. Bending of Long Steel and Aluminum Rods During End Impact With a Rigid Target. *J. Mech. Engng. Sci.* **1981**, *23* (2), 85–92.

6. Johnson, W.; Sengupta, A. K.; Ghosh, S. K. Plasticine Modelled High Velocity Oblique Impact and Ricochet of Long Rods. *Int. J. Mech. Sci.* **1982**, *24* (7), 437–455.

7. Johnson, W.; Reid, S. R.; Sengupta, A. K.; Ghosh, S. K. Modelling With Plasticine the Low Speed Impact of Long Rods Against Inclined Rigid Targets. *Int. J. Impact Engng.* **1983**, *1* (1), 73–83.

8. Rosenberg, Z.; Yeshurun, Y.; Mayseless, M. On the Ricochet of Long Rod Projectiles. *Proceedings of the 11th International Symposium on Ballistics*, Brussels, Belgium, **1989**.

9. Orphal, D. L.; Anderson, C. E., Jr. Test Damage From Highly Oblique Impacts of Steel Spheres Against Thin Laminated Targets. *Int. J. Impact Engng.* **2001**, *26*, 567–578.

10. Roisman, I. V.; Yarin, A. L.; Rubin, M. B. Oblique Penetration of a Rigid Projectile Into an Elastic-Plastic Target. *Int. J. Impact Engng.* **1997**, *19*, 769–795.

11. Zukas, J. A.; Gaskill, B. Ricochet of Deforming Projectiles From Deforming Plates. *Int. J. Impact Engng.* **1996**, *18*, (*6*), 601–610.

12. Gupta, N. K.; Madhu, V. An Experimental Study of Normal and Oblique Impact of Hard-Core Projectile on Single and Layered Plates. *Int. J. Impact Engng.* **1997**, *19*, 395–414.

13. Schonberg, W. P. Characterizing Secondary Debris Impact Ejecta. *Int. J. Impact Engng.* **2001**, 26, 713–724.

14. Segletes, S. B.; Grote, R.; Polesne, J. *Improving the Rod-Penetration Algorithm for Tomorrow's Armors*; ARL-RP-23; U.S. Army Research Laboratory: Aberdeen Proving Ground, MD, **2001**.

15. Segletes, S. B. *An Adaptation of Walker-Anderson Model Elements Into The Frank-Zook Penetration Model for Use in MUVES*; ARL-TR-2336; U.S. Army Research Laboratory: Aberdeen Proving Ground, MD, **2000**.

NO. OF COPIES	ORGANIZATION
1 (PDF Only)	DEFENSE TECHNICAL INFORMATION CTR DTIC OCA 8725 JOHN J KINGMAN RD STE 0944 FT BELVOIR VA 22060-6218
1	COMMANDING GENERAL US ARMY MATERIEL CMD AMCRDA TF 5001 EISENHOWER AVE ALEXANDRIA VA 22333-0001
1	INST FOR ADVNCD TCHNLGY THE UNIV OF TEXAS AT AUSTIN 3925 W BRAKER LN STE 400 AUSTIN TX 78759-5316
1	US MILITARY ACADEMY MATH SCI CTR EXCELLENCE MADN MATH THAYER HALL WEST POINT NY 10996-1786
1	DIRECTOR US ARMY RESEARCH LAB AMSRD ARL CS IS R 2800 POWDER MILL RD ADELPHI MD 20783-1197
3	DIRECTOR US ARMY RESEARCH LAB AMSRD ARL CI OK TL 2800 POWDER MILL RD ADELPHI MD 20783-1197
3	DIRECTOR US ARMY RESEARCH LAB AMSRD ARL CS IS T 2800 POWDER MILL RD ADELPHI MD 20783-1197

NO. OF COPIES	ORGANIZATION
	ABERDEEN PROVING GROUND
1	DIR USARL AMSRD ARL CI OK TP (BLDG 4600)

NO. OF COPIES ORGANIZATION

4 DEFENSE THREAT REDUCTION AGENCY
J LYON
K HUNTER
T FREDERICKSON
R LAWRENCE
8725 JOHN J KINGMAN RD
STOP 6201
FT BELVOIR VA 22060-6201

2 COMMANDER
US ARMY ARDEC
AMSTA AR FSA E
W P DUNN
E BAKER
PICATINNY ARSENAL NJ 07806-5000

1 COMMANDER
US ARMY ARDEC
AMSTA AR CCH V M D NICOLICH
PICATINNY ARSENAL NJ 07806-5000

1 COMMANDER
US ARMY ARDEC
E ANDRICOPOULOS
PICATINNY ARSENAL NJ 07806-5000

1 COMMANDER
USA STRATEGIC DEFNS CMD
CSSD H LL T CROWLES
HUNTSVILLE AL 35807-3801

4 COMMANDER
US ARMY AVIATION & MISSLE CMD
AMSAM RD PS WF
S HILL
D LOVELACE
M SCHEXNAYDER
G SNYDER
REDSTONE ARSENAL AL 35898-5247

1 COMMANDER
US ARMY AVIATION & MISSLE CMD
AMSAM RD SS AA
J BILLINGSLEY
REDSTONE ARSENAL AL 35898

1 MIS DEFNS & SPACE TECHNOLOGY
CSSD SD T K H JORDAN
PO BOX 1500
HUNTSVILLE AL 34807-3801

NO. OF COPIES ORGANIZATION

3 COMMANDER
US ARMY RESEARCH OFFICE
K IYER
J BAILEY
S DAVIS
PO BOX 12211
RESEARCH TRIANGLE PARK NC
27709-2211

1 NAVAL AIR WARFARE CTR
S A FINNEGAN
BOX 1018
RIDGECREST CA 93556

4 COMMANDER
NAVAL WEAPONS CENTER
N FASIG CODE 3261
T YEE CODE 3263
D THOMPSON CODE 3268
W MCCARTER CODE 6214
CHINA LAKE CA 93555

12 COMMANDER
NAVAL SURFACE WARFARE CTR
DAHLGREN DIVISION
H CHEN
D DICKINSON CODE G24
C ELLINGTON
C GARRETT CODE G22
W HOLT CODE G22
W HOYE G22
R MCKEOWN
J NELSON
M SILL CODE H11
W STROTHER
A WARDLAW JR
L WILLIAMS CODE G33
17320 DAHLGREN RD
DAHLGREN VA 22448

2 AIR FORCE ARMAMENT LAB
AFATL DLJR
J FOSTER
D LAMBERT
EGLIN AFB FL 32542-6810

1 USAF PHILLIPS LABORATORY
VTSI
ROBERT ROYBAL
KIRTLAND AFB NM 87117-7345

1 AFIT ENC
D FULK
WRIGHT PATTERSON AFB OH 45433

NO. OF COPIES	ORGANIZATION
1	FBI FBI LAB EXPLOSIVES UNIT M LEONE 935 PENNSYLVANIA AVE NW WASHINGTON DC 20535
6	LOS ALAMOS NATIONAL LABORATORY L HULL MS A133 J V REPA MS A133 J WALTER MS C305 E J CHAPYAK MS F664 P HOWE MS P915 J KENNEDY MS P915 PO BOX 1663 LOS ALAMOS NM 87545
30	SNL MS 0100 J ANG MS0310 P YARRINGTON MS0310 A ROBINSON ORG9231 MS0378 W TEDESCHI MS0479 B LEVIN MS0706 T TRUCANO MS0819 P TAYLOR MS0820 R BRANNON MS0820 M KIPP MS0820 D CRAWFORD MS0820 L CHHABILDAS MS0821 P STANTON MS0821 J MCGLAUN MS0835 E HERTEL JRMS0836 L KMETYK MS0980 J SOUTHWARD MS0980 R LAFARGE MS0986 R TACHAU MS1156 M FURNISH MS1168 M FORRESTAL MS1174 W REINHART MS1181 D HAYES MS1181 J ASAY MS1181 E REECE MS1185 D KELLY MS1185 C HALL MS1209 J COREY MS1217 C HILLS MS1411 M VIGIL MS1454 R NELLUMS PO BOX 5800 ALBUQUERQUE NM 87185-0100

NO. OF COPIES	ORGANIZATION
31	DIR LLNL MS L35 R TIPTON D BAUM M MURPHY T MCABEE MS L122 R PIERCE R ROSINKY O ALFORD D STEWART T VIDLAK B BOWMAN W DIXON MS L125 D FAUX N KLINO MS L149 R VAROSH R BARKER L159 MS L163 M FINGER R PERRET W SHOTTS MS L178 H KRUGER G POMYKAL M GERASSIMENKO MS L180 G SIMONSON A SPERO F HANDLER L182 MS L282 W TAO MS L290 A HOLT J REAUGH S COCHRAN L389 MS L495 D GAVEL J HUNTER R KUKLO L874 PO BOX 808 LIVERMORE CA 94550

NO. OF COPIES ORGANIZATION

4 ENERGETIC MATERIALS
RSCH TSTNG CTR
NEW MEXICO TECH
D CHAVEZ
L LIBERSKY
F SANDSTROM
M STANLEY
CAMPUS STATION
SOCORRO NM 87801

3 NASA
JOHNSON SPACE CTR
E CHRISTIANSEN
J CREWS
F HORZ
MAIL CODE SN3
2101 NASA RD 1
HOUSTON TX 77058

1 APPLIED RESEARCH LAB
J COOK
10000 BURNETT RD
AUSTIN TX 78758

5 JET PROPULSION LABORATORY
IMPACT PHYSICS GROUP
Z SEKANINA
P WEISSMAN
B WEST
J ZWISSLER
M ADAMS
4800 OAK GROVE DR
PASADENA CA 91109

2 CALTECH
J SHEPHERD MS 105 50
A INGERSOLL MS 170 25
1201 E CALIFORNIA BLVD
PASADENA CA 91125

1 DREXEL UNIVERSITY
MEM DEPT
32ND AND CHESTNUT ST
PHILADELPHIA PA 19104

1 GEORGIA INSTITUTE
OF TECHNOLOGY
COMPUTATIONAL MODELING CTR
S ATLURI
ATLANTA GA 30332-0356

NO. OF COPIES ORGANIZATION

5 JOHNS HOPKINS UNIVERSITY
APPLIED PHYSICS LAB
T BETZER
A EATON
R KEITH
D PACE
R WEST
JOHNS HOPKINS RD
LAUREL MD 20723

1 LOUISIANA STATE UNIVERSITY
R COURTER
948 WYLIE DR
BATON ROUGE LA 70808

4 SOUTHWEST RESEARCH INSTITUTE
C ANDERSON
S MULLIN
J RIEGEL
J WALKER
PO DRAWER 28510
SAN ANTONIO TX 78228-0510

1 SUNY STONEYBROOK
DEPT APPL MATH AND STAT
J GLIMM
STONEYBROOK NY 11794

2 UC SAN DIEGO
DEPT APPL MECH AND ENGNG
SVCS R011
S NEMAT-NASSER
M MEYERS
LA JOLLA CA 92093-0411

2 UNIV OF ALA HUNTSVILLE
AEROPHYSICS RSCH CTR
G HOUGH
D LIQUORNIK
PO BOX 999
HUNTSVILLE AL 35899

1 UNIV OF ALA HUNTSVILLE
MECH ENGRNG DEPT
W SCHONBERG
HUNTSVILLE AL 35899

2 UNIVERSITY OF DAYTON RSCH INST
N BRAR
A PIEKUTOWSKI
300 COLLEGE PARK
DAYTON OH 45469-0182

NO. OF COPIES ORGANIZATION

3 UNIVERSITY OF DELAWARE
DEPT OF MECH ENGNG
J GILLESPIE
J VINSON
D WILKINS
NEWARK DE 19716

1 UNIVERSITY OF ILLINOIS
PHYSICS BLDG
A GRANATO
URBANA IL 61801

1 UNIVERSITY OF TEXAS
DEPT OF MECH ENGNG
E FAHRENTHOLD
AUSTIN TX 78712

1 VIRGINIA POLYTECHNIC INSTITUTE
COLLEGE OF ENGNG
DEPT ENGNG SCIENCE AND MECHANICS
R BATRA
BLACKSBURG VA 24061-0219

2 AEROJET
J CARLEONE
S KEY
PO BOX 13222
SACRAMENTO CA 95813-6000

2 AEROJET ORDNANCE
P WOLF
G PADGETT
1100 BULLOCH BLVD
SOCORRO NM 87801

1 M L ALME
2180 LOMA LINDA DR
LOS ALAMOS NM 87544-2769

1 APPLIED RESEARCH ASSOC INC
J YATTEAU
5941 S MIDDLEFIELD RD STE 100
LITTLETON CO 80123

2 APPLIED RESEARCH ASSOC INC
D GRADY
F MAESTAS
SUITE A220
4300 SAN MATEO BLVD NE
ALBUQUERQUE NM 87110

NO. OF COPIES ORGANIZATION

1 APPLIED RESEARCH LABORATORIES
T M KIEHNE
PO BOX 8029
AUSTIN TX 78713-8029

1 ATA ASSOCIATES
W ISBELL
PO BOX 6570
SANTA BARBARA CA 93111

1 BRIGS CO
J BACKOFEN
2668 PETERSBOROUGH ST
HERNDON VA 20171-2443

1 CENTURY DYNAMICS INC
N BIRNBAUM
1001 GALAXY WAY
SUITE 325
CONCORD CA 94583-1613

1 COMPUTATIONAL MECHANICS CONSULTANTS
J ZUKAS
PO BOX 11314
BALTIMORE MD 21239-0314

3 DOW CHEMICAL INC
ORDNANCE SYSTEMS
C HANEY
A HART
B RAFANIELLO
800 BLDG
MIDLAND MI 48667

3 DE TECHNOLOGIES INC
P CHOU
R CICCARELLI
W FLIS
3620 HORIZON DR
KING OF PRUSSIA PA 19406

3 DYNASEN
J CHAREST
M CHAREST
M LILLY
20 ARNOLD PL
GOLETA CA 93117

NO. OF COPIES	ORGANIZATION
1	R J EICHELBERGER 409 W CATHERINE ST BEL AIR MD 21014-3613
1	ELORET INSTITUTE D BOGDANOFF MS 230 2 NASA AMES RESEARCH CTR MOFFETT FIELD CA 94035
1	GB TECH LOCKHEED J LAUGHMAN 2200 SPACE PARK STE 400 HOUSTON TX 77258
2	GB TECH LOCKHEED L BORREGO C23C J FALCON JR C23C 2400 NASA RD 1 HOUSTON TX 77058
6	GDLS 38500 MOUND RD W BURKE MZ436 21 24 G CAMPBELL MZ436 30 44 D DEBUSSCHER MZ436 20 29 J ERIDON MZ436 21 24 W HERMAN MZ 435 01 24 S PENTESCU MZ436 21 24 STERLING HTS MI 48310-3200
1	GENERAL RESEARCH CORP T MENNA PO BOX 6770 SANTA BARBARA CA 93160-6770
1	RAYTHEON MSL SYS CO T STURGEON BLDG 805 MS D4 PO BOX 11337 TUCSON AZ 85734-1337
5	INST FOR ADVANCED TECHNOLOGY S J BLESS J CAZAMIAS J DAVIS H FAIR D LITTLEFIELD 3925 W BRAKER LN STE 400 AUSTIN TX 78759-5316
1	INTERNATIONAL RESEARCH ASSOC D ORPHAL 4450 BLACK AVE PLEASANTON CA 94566

NO. OF COPIES	ORGANIZATION
2	ITT SCIENCES AND SYSTEMS J WILBECK J KILPATRICK 600 BLVD SOUTH STE 208 HUNTSVILLE AL 35802
1	KAMAN SCIENCES CORP D JONES 2560 HUNTINGTON AVE STE 200 ALEXANDRIA VA 22303
7	KAMAN SCIENCES CORP J ELDER R HENDERSON D PYLES F SAVAGE J A SUMMERS T MOORE T YEM 600 BLVD S STE 208 HUNTSVILLE AL 35802
1	D R KENNEDY AND ASSOC INC D KENNEDY PO BOX 4003 MOUNTAIN VIEW CA 94040
1	LOCKHEED MARTIN ELEC AND MSLS G W BROOKS 5600 SAND LAKE RD MP 544 ORLANDO FL 32819-8907
1	LOCKHEED MARTIN MISSILE & SPACE W EBERLE PO BOX 070017 HUNTSVILLE AL 35807
3	LOCKHEED MISSILE AND SPACE CO M LEVIN ORG 81 06 BLDG 598 M MCHENRY T A NGO ORG 81 10 BLDG 157 111 LOCKHEED WAY SUNNYVALE CA 94088
4	LOCKHEED MISSILE AND SPACE CO J ANDERSON W KNUDSON S KUSUMI 0 81 11 BLDG 157 J PHILLIPS 0 54 50 PO BOX 3504 SUNNYVALE CA 94088

NO. OF COPIES ORGANIZATION

1 LOCKHEED MISSILE AND SPACE CO
R HOFFMAN
SANTA CRUZ FACILITY
EMPIRE GRADE RD
SANTA CRUZ CA 95060

1 MCDONNELL DOUGLAS
ASTRONAUTICS CO
B COOPER
5301 BOLSA AVE
HUNTINGTON BEACH CA 92647

2 NETWORK COMPUTING
SERVICES INC
T HOLMQUIST
G JOHNSON
1200 WASHINGTON AVE S
MINNEAPOLIS MN 55415

3 GD OTS
D MATUSKA
M GUNGER
J OSBORN
4565 COMMERCIAL DR A
NICEVILLE FL 32578

1 PHYSICAL SCIENCES INC
P NEBOLSINE
20 NEW ENGLAND BUS CTR
ANDOVER MA 01810

2 GD OTS
D BOEKA
N OUYE
400 ESTUDILLO AVE
STE 100
SAN LEANDRO CA 94577-0205

1 RAYTHEON ELECTRONIC SYSTEMS
R LLOYD
50 APPLE HILL DR
TEWKSBURY MA 01876

1 ROCKWELL INTERNATIONAL
ROCKETDYNE DIV
H LEIFER
16557 PARK LN CIRCLE
LOS ANGELES CA 90049

1 SAIC
M W MCKAY
10260 CAMPUS POINT DR
SAN DIEGO CA 92121

NO. OF COPIES ORGANIZATION

1 SHOCK TRANSIENTS INC
D DAVISON
BOX 5357
HOPKINS MN 55343

1 J STERNBERG
20 ESSEX LN
WOODBURY CT 06798

2 SOUTHERN RESEARCH INSTITUTE
L DECKARD
D SEGERS
PO BOX 55305
BIRMINGHAM AL 35255-5305

5 SRI INTERNATIONAL
J COLTON
D CURRAN
R KLOOP
R SEAMAN
D A SHOCKEY
333 RAVENSWOOD AVE
MENLO PARK CA 94025

1 BAE SYSTEMS ANALYTICAL
SOLUTIONS
M RICHARDSON
1525 PERIMETER PKWY STE 500
HUNTSVILLE AL 35806

1 ZERNOW TECHNICAL SVCS INC
L ZERNOW
425 W BONITA AVE STE 208
SAN DIMAS CA 91773

1 R JAMESON
624 ROWE DR
ABERDEEN MD 21001

ABERDEEN PROVING GROUND

70 DIR USARL
AMSRD ARL SL B
P TANENBAUM
AMSRD ARL SL BB
D BELY
G BRADLEY
M BURDESHAW
R DIBELKA
E HUNT
D FARENWALD
D DIETRICH
M O'MALLEY
J ROBERTSON

NO. OF COPIES	ORGANIZATION
	AMSRD ARL SL BD
	R GROTE
	L MOSS
	J POLESNE
	AMSRD ARL WM BC
	A ZIELINSKI
	AMSRD ARL WM BE
	R SAUCIER
	AMSRD ARL WM MB
	W DEROSSET
	G GAZONAS
	C HOPPEL
	AMSRD ARL WM MC
	E CHIN
	J LASALVIA
	AMSRD ARL WM T
	B BURNS
	T W WRIGHT
	W GILLICH
	AMSRD ARL WM TA
	M ZOLTOSKI
	T HAVEL
	M BURKINS
	N GNIAZDOWSKI
	W A GOOCH
	E HORWATH
	D KLEPONIS
	B LEAVY
	M NORMANDIA
	J RUNYEON
	G SILSBY
	AMSRD ARL WM TB
	P BAKER
	R BITTING
	R LOTTERO
	J STARKENBERG
	AMSRD ARL WM TC
	R COATES
	J BARB
	N BRUCHEY
	M FERMEN-COKER
	E KENNEDY
	K KIMSEY
	L MAGNESS
	D SCHEFFLER
	S SCHRAML
	B SORENSEN
	R SUMMERS
	W WALTERS
	G RANDERS-PEHRSON LLNL

NO. OF COPIES	ORGANIZATION
	AMSRD ARL WM TD
	S SCHOENFELD
	S R BILYK
	T W BJERKE
	D CASEM
	J CLAYTON
	D DANDEKAR
	Y I HUANG
	K IYER
	H KANG
	H W MEYER
	M RAFTENBERG
	AMSRD ARL WM TD
	E RAPACKI
	M SCHEIDLER
	S SEGLETES (3 CPS)
	T WEERISOORIYA
	AMSRD ARL WM TE
	J POWELL
	A PRAKASH

NO. OF COPIES	ORGANIZATION
2	AERONAUTICAL AND MARITIME RESEARCH LABORATORY S CIMPOERU D PAUL PO BOX 4331 MELBOURNE VIC 3001 AUSTRALIA
1	DSTO AMRL WEAPONS SYSTEMS DIVISION N BURMAN (RLLWS) SALISBURY SOUTH AUSTRALIA 5108 AUSTRALIA
1	ROYAL MILITARY ACADEMY G DYCKMANS RENAISSANCELAAN 30 1000 BRUSSELS BELGIUM
1	BULGARIAN ACADEMY OF SCIENCES SPACE RESEARCH INSTITUTE V GOSPODINOV 1000 SOFIA PO BOX 799 BULGARIA
1	CANADIAN ARSENALS LTD P PELLETIER 5 MONTEE DES ARSENAUX VILLIE DE GRADEUR PQ J5Z2 CANADA
1	DEFENCE RSCH ESTAB SUFFIELD D MACKAY RALSTON ALBERTA TOJ 2NO RALSTON CANADA
1	DEFENCE RSCH ESTAB SUFFIELD C WEICKERT BOX 4000 MEDICINE HAT ALBERTA TIA 8K6 CANADA
1	DEFENCE RSCH ESTAB VALCARTIER ARMAMENTS DIVISION R DELAGRAVE 2459 PIE X1 BLVD N PO BOX 8800 CORCELETTE QUEBEC GOA 1R0 CANADA

NO. OF COPIES	ORGANIZATION
1	CEA R CHERET CEDEX 15 313 33 RUE DE LA FEDERATION PARIS 75752 FRANCE
1	CEA CESTA A GEILLE BOX 2 LE BARP 33114 FRANCE
5	CENTRE D'ETUDES DE GRAMAT C LOUPIAS P OUTREBON J CAGNOUX C GALLIC J TRANCHET GRAMAT 46500 FRANCE
6	CENTRE DE RECHERCHES ET D'ETUDES D'ARCUEIL D BOUVART C COTTENNOT S JONNEAUX H ORSINI S SERROR F TARDIVAL 16 BIS AVENUE PRIEUR DE LA COTE D'OR F94114 ARCUEIL CEDEX FRANCE
1	DAT ETBS CETAM C ALTMAYER ROUTE DE GUERRY BOURGES 18015 FRANCE
1	ETBS DSTI P BARNIER ROUTE DE GUERAY BOITE POSTALE 712 18015 BOURGES CEDEX FRANCE
1	FRENCH GERMAN RESEARCH INST P-Y CHANTERET CEDEX 12 RUE DE I'INDUSTRIE BP 301 F68301 SAINT-LOUIS FRANCE

NO. OF COPIES	ORGANIZATION
5	FRENCH GERMAN RESEARCH INST H-J ERNST F JAMET P LEHMANN K HOOG H F LEHR CEDEX 5 5 RUE DU GENERAL CASSAGNOU SAINT LOUIS 68301 FRANCE
1	CONDAT J KIERMEIR MAXIMILIANSTR 28 8069 SCHEYERN FERNHAG GERMANY
1	TDW M HELD POSTFACH 13 40 D 86523 SCHROBENHAUSEN GERMANY
1	DIEHL GBMH AND CO M SCHILDKNECHT FISCHBACHSTRASSE 16 D 90552 ROETBENBACH AD PEGNITZ GERMANY
4	ERNST MACH INSTITUT V HOHLER E SCHMOLINSKE E SCHNEIDER K THOMA ECKERSTRASSE 4 D 7800 FREIBURG I BR 791 4 GERMANY
3	FRAUNHOFER INSTITUT FUER KURZZEITDYNAMIK ERNST MACH INST H ROTHENHAEUSLER H SENF E STRASSBURGER KLINGELBERG 1 D79588 EFRINGEN KIRCHEN GERMANY

NO. OF COPIES	ORGANIZATION
3	FRENCH GERMAN RESEARCH INST G WEIHRAUCH R HUNKLER E WOLLMANN POSTFACH 1260 WEIL AM RHEIN D 79574 GERMANY
2	IABG M BORRMANN H DORSCH EINSTEINSTRASSE 20 D 8012 OTTOBRUN B MUENCHEN GERMANY
1	INGENIEURBUERO DEISENROTH AUF DE HARDT 33 35 D5204 LOHMAR 1 GERMANY
1	NATIONAL GEOPHYSICAL RESEARCH INSTITUTE G PARTHASARATHY HYDERABAD-500 007 (A P) INDIA
5	RAFAEL BALLISTICS CTR E DEKEL Y PARTOM G ROSENBERG Z ROSENBERG Y YESHURUN PO BOX 2250 HAIFA 31021 ISRAEL
1	SOREQ NUCLEAR RESEARCH CENTRE ISRAEL ATOMIC ENERGY COMMISSION Z JAEGER 81800 YAVNE ISRAEL
1	TECHNION INST OF TECH FACULTY OF MECH ENGNG S BODNER TECHNION CITY HAIFA 32000 ISRAEL

NO. OF COPIES ORGANIZATION

1 ESTEC CS
D CASWELL
BOX 200 NOORDWIJK
2200 AG
NETHERLANDS

2 EUROPEAN SPACE AGENCY ESTEC
L BERTHOUD
M LAMBERT
POSTBUS BOX 299 NOORDWIJK
NL2200 AG
NETHERLANDS

4 PRINS MAURITS LABORATORY
H REITSMA
E VAN RIET
H PASMAN
R YSSELSTEIN
TNO BOX 45
RIJSWIJK 2280AA
NETHERLANDS

1 ROYAL NETHERLANDS ARMY
J HOENEVELD
V BURCHLAAN 31
PO BOX 90822
2509 LS THE HAGUE
NETHERLANDS

1 INSTITUTE OF PHYSICS
SILESIAN TECH UNIVERSITY
E SOCZKIEWICZ
44 100 GLIWICE
UL KRZYWOUSTEGO 2
POLAND

1 INST OF CHEM PHYS
A YU DOLGOBORODOV
KOSYGIN ST 4 V 334
MOSCOW
RUSSIA

4 INST OF CHEM PHYS
RUSSIAN ACADEMY OF SCIENCES
G KANEL
A MOLODETS
S AZORENOV
A UTKIN
142432 CHERNOGOLOVKA
MOSCOW REGION
RUSSIA

NO. OF COPIES ORGANIZATION

1 INSTITUTE OF EARTH'S CRUST
P I DOROGOKUPETS
664033 IRKUTSK
RUSSIA

3 INSTITUTE OF MECH ENGNG PROBLEMS
V BULATOV
D INDEITSEV
Y MESCHERYAKOV
BOLSHOY 61 VO
ST PETERSBURG 199178
RUSSIA

1 INSTITUTE OF MINEROLOGY AND PETROGRAPHY
V DREBUSHCHAK
UNIVERSITETSKI PROSPEKT 3
630090 NOVOSIBIRSK
RUSSIA

2 IOFFE PHYSICO TECHNICAL INSTITUTE
DENSE PLASMA DYNAMICS LABORATORY
E DROBYSHEVSKI
A KOZHUSHKO
ST PETERSBURG 194021
RUSSIA

1 IPE RAS
A BOGOMAZ
DVORTSOVAIA NAB 18
ST PETERSBURG
RUSSIA

2 LAVRENTYEV INST HYDRODYNAMICS
L MERZHIEVSKY
V SILVESTROV
630090 NOVOSIBIRSK
RUSSIA

1 MOSCOW INST OF PHYS AND TECH
S UTYUZHNIKOV
DEPT OF COMPUTATIONAL MATHEMATICS
DOLGOPRUDNY 1471700
RUSSIA

NO. OF COPIES ORGANIZATION

1 RESEARCH INST
OF MECH
NIZHNIY NOVGOROD
STATE UNIVERSITY
A SADYRIN
P GAYARINA 23 KORP 6
NIZHNIY NOVGOROD 603600
RUSSIA

2 RUSSIAN FEDERAL NUCLEAR
CENTER VNIIEF
L F GUDARENKO
R F TRUNIN
MIRA AVE 37
SAROV 607190
RUSSIA

1 ST PETERSBURG STATE
TECHNICAL UNIVERSITY
FACULTY OF PHYSICS
AND MECHANICS
DEPT OF THEORETICAL MECHANICS
ATTN A KRIVTSOV
POLITECHNICHESKAYA ST 29
195251 ST PETERSBURG
RUSSIA

1 SAMARA STATE AEROSPACE UNIV
L LUKASHEV
SAMARA
RUSSIA

1 UNIVERSIDAD DE CANTABRIA
FACULTAD DE CIENCIAS
DEPARTMENTO DE FISICA
APLICADA
J AMOROS
AVDA DE LOS CASTROS S/N
39005 SANTANDER
SPAIN

1 DYNAMEC RESEARCH
A PERSSON
PO BOX 201
S 151 23 SODERTALJE
SWEDEN

NO. OF COPIES ORGANIZATION

7 FOI
SWEDISH DEFENCE
RESEARCH AGENCY
GRINDSJON RESEARCH CENTRE
L GUNNAR OLSSON
B JANZON
G WIJK
R HOLMLIN
C LAMNEVIK
L FAST
M JACOB
SE 147 25 TUMBA
SWEDEN

2 SWEDISH DEFENCE RSCH ESTAB
DIVISION OF MATERIALS
S J SAVAGE
J ERIKSON
STOCKHOLM S 17290
SWEDEN

2 K AND W THUN
W LANZ
W ODERMATT
ALLMENDSSTRASSE 86
CH 3602 THUN
SWITZERLAND

2 AWE
M GERMAN
W HARRISON
FOULNESS ESSEX SS3 9XE
UK

1 CENTURY DYNAMICS LTD
N FRANCIS
DYNAMICS HOUSE
HURST RD
HORSHAM
WEST SUSSEX RH12 2DT
UK

5 DERA
I CULLIS
J P CURTIS Q13
A HART Q13
K COWAN Q13
M FIRTH R31
FORT HALSTEAD
SEVENOAKS KENT TN14 7BP
UK

NO. OF
COPIES ORGANIZATION

1 UK MINISTRY OF DEFENCE
G CAMBRAY
CBDE PORTON DOWN SALISBURY
WITTSHIRE SPR 0JQ
UK

2 UNIVERSITY OF KENT
PHYS LABORATORY
UNIT FOR SPACE SCIENCES
P GENTA
P RATCLIFF
CANTERBURY KENT CT2 7NR
UK

7 INST FOR PROBLEMS IN
MATERIALS SCIENCE
S FIRSTOV
B GALANOV
O GRIGORIEV
V KARTUZOV
V KOVTUN
Y MILMAN
V TREFILOV
3 KRHYZHANOVSKY STR
252142 KIEV 142
UKRAINE

1 INSTITUTE FOR PROBLEMS
OF STRENGTH
G STEPANOV
TIMIRYAZEVSKAYU STR 2
252014 KIEV
UKRAINE

INTENTIONALLY LEFT BLANK.